The ASPIICS solar coronagraph aboard the Proba-3 formation flying mission

Scientific objectives and instrument design

A. N. Zhukov[1], C. Thizy[2], D. Galano[3], B. Bourgoignie[1], L. Dolla[1], C. Jean[1], B. Nicula[1], S. Shestov[1,2], C. Galy[2], R. Rougeot[3], J. Versluys[3], J. Zender[3], P. Lamy[4], S. Fineschi[5], S. Gunár[6], B. Inhester[7], M. Mierla[1,8], P. Rudawy[9], K. Tsinganos[10], S. Koutchmy[11]⋆, R. Howard[12], H. Peter[7], S. Vivès[13], L. Abbo[5], C. Aime[14], K. Aleksiejuk[15], J. Baran[15], U. Bąk-Stęślicka[9], A. Bemporad[5], D. Berghmans[1], D. Beşliu-Ionescu[16,8], S. Buckley[17], O. Buiu[18], G. Capobianco[5], I. Cimoch[19], E. D'Huys[1], M. Dzieżyc[20], K. Fleury-Frenette[2], S. E. Gibson[21], S. Giordano[5], L. Golub[22], K. Grochowski[20], P. Heinzel[6,9], A. Hermans[2], J. Jacobs[2], S. Jejčič[23,24,6], N. Kranitis[10], F. Landini[5], D. Loreggia[5], J. Magdalenić[1,25], D. Maia[26], C. Marqué[1], R. Melich[27], M. Morawski[15], M. Mosdorf[20], V. Noce[5], P. Orleański[15], A. Paschalis[10], R. Peřestý[28], L. Rodriguez[1], D. B. Seaton[29], L. Short[1], J.-F. Simar[2], M. Stęślicki[15], R. Sørensen[30], G. Terrasa[2], N. Van Vooren[30], F. Verstringe[1], and L. Zangrilli[5]

[1] Solar–Terrestrial Centre of Excellence — SIDC, Royal Observatory of Belgium, 1180 Brussels, Belgium
   e-mail: `Andrei.Zhukov@sidc.be`
[2] Centre Spatial de Liège, Université de Liège, Av. du Pré-Aily B29, 4031 Angleur, Belgium
[3] European Space Research and Technology Centre, European Space Agency, Noordwijk, Netherlands
[4] Laboratoire Atmosphéres et Observations Spatiales, 11 Boulevard d'Alembert, 78280 Guyancourt, France
[5] National Institute for Astrophysics, Astrophysical Observatory of Torino, Pino Torinese, Torino, Italy
[6] Astronomical Institute of the Czech Academy of Sciences, 251 65 Ondřejov, Czech Republic
[7] Max Planck Institute for Solar System Research, Justus-von-Liebig-Weg 3, 37077 Göttingen, Germany
[8] Institute of Geodynamics of the Romanian Academy, 020032 Bucharest-37, Romania
[9] Astronomical Institute, University of Wrocław, Kopernika 11, 51-622 Wrocław, Poland
[10] University of Athens, Panepistimiopolis, 157 84 Zografos Athens, Greece
[11] Institut d'Astrophysique de Paris, Paris, France
[12] Applied Physics Laboratory, Johns Hopkins University, USA
[13] IRFM, CEA, F-13108 Saint Paul lez Durance, France
[14] Université Côte d'Azur, Centre National de la Recherche Scientifique, Observatoire de la Côte d'Azur, UMR7293 Lagrange, Parc Valrose, 06108, Nice, France
[15] Centrum Badań Kosmicznych Polskiej Akademii Nauk, Poland
[16] Astronomical Institute of the Romanian Academy, Bucharest, Romania
[17] Onsemi, Cork, Ireland
[18] National Institute for Research & Development in Microtechnologies, Bucharest, Romania
[19] PCO S.A., Warsaw, Poland
[20] N7 Space Sp. z o. o., Warsaw, Poland
[21] High Altitude Observatory, National Center for Atmospheric Research, Boulder, CO, USA
[22] Harvard-Smithsonian Center for Astrophysics, USA
[23] Faculty of Education, University of Ljubljana, 1000, Ljubljana, Slovenia
[24] Faculty of Mathematics and Physics, University of Ljubljana, 1000 Ljubljana, Slovenia
[25] Center for mathematical Plasma Astrophysics, KU Leuven, Leuven 3000, Belgium
[26] Faculty of Sciences, Porto University, Porto, Portugal
[27] Institute of Plasma Physics ASCR v.v.i. (TOPTEC), Turnov, Czech Republic
[28] Serenum a.s., Praha, Czech Republic
[29] Southwest Research Institute, Boulder, CO 80302, USA
[30] OIP Sensor Systems n.v., Oudenaarde, Belgium

ABSTRACT

We describe the scientific objectives and instrument design of the ASPIICS coronagraph launched aboard the Proba-3 mission of the European Space Agency (ESA) on 5 December 2024. Proba-3 consists of two spacecraft in a highly elliptical orbit around the Earth. One spacecraft carries the telescope, and the external occulter is mounted on the second spacecraft. The two spacecraft fly in a precise formation during 6 hours out of 19.63 hour orbit, together forming a giant solar coronagraph called ASPIICS (Association of Spacecraft for Polarimetric and Imaging Investigation of the Corona of the Sun). Very long distance between the external occulter and the telescope (around 144 m) represents an increase of two orders of magnitude compared to classical externally occulted solar coronagraphs. This allows us to observe the inner corona in eclipse-like conditions, i.e. close to the solar limb (down to $1.099\,R_\odot$) and with very low straylight. ASPIICS will provide a new perspective on the inner solar corona that will help solve several outstanding problems in solar physics, such as the origin of the slow solar wind and physical mechanism of coronal mass ejections.

Key words. Instrumentation: miscellaneous – Space vehicles – Sun: corona – solar wind – Sun: coronal mass ejections (CMEs)

1. Introduction

The solar corona is the outer part of the solar atmosphere. It is very hot (1–2 MK) compared to the photospheric temperature of 5770 K. The corona is continuously expanding into interplanetary space in the form of the solar wind. Occasionally, eruptive energy release events in the solar atmosphere lead to coronal mass ejections (CMEs). The origin of the solar wind and the initiation of CMEs are fundamental scientific questions that are still not fully resolved.

When arriving at Earth, solar wind streams and especially CMEs may disturb the geomagnetic field and produce a geomagnetic storm. CME-driven shocks also accelerate energetic particles, which represent a danger to astronauts traveling to the Moon and Mars (Schwenn 2006; Bothmer & Zhukov 2007; Temmer 2021). These effects, collectively called "space weather", make studies of the solar corona important for practical applications as well.

The solar corona has been observed for millennia during total solar eclipses. The near-coincidence of apparent sizes of the Sun and Moon makes a total eclipse possible. However, this also means that an eclipse is rather short: 7 minutes and 40 seconds at most, and typically 2–3 minutes. During a few minutes of totality, the corona rarely shows any dynamical evolution. The misalignment of the Moon's orbit around Earth with respect to the Earth's orbit around the Sun makes total eclipses rare: at most two per year, usually one per year, and none in some years.

Modern remote-sensing observations of the corona are generally made using two techniques[1]. The first technique is to observe the lower corona in extreme ultraviolet (EUV) or X-ray emission. In this case, the corona is observed not only above the limb but also against the solar disk. The field of view is typically limited to less than 1.5 $R_\odot$ (where $R_\odot$ is the solar radius and the distance is measured from the Sun's center): 1.27 $R_\odot$ for the Atmospheric Imaging Assembly (AIA, see Lemen et al. 2012) aboard the Solar Dynamics Observatory mission (SDO, see Pesnell et al. 2012), and 1.67 $R_\odot$ for the Solar Watcher using Active Pixel sensor (SWAP, see Berghmans et al. 2006; Seaton et al. 2013) aboard the PROBA2 mission.

The second technique is to observe the high corona with externally occulted coronagraphs, such as LASCO C2 (Large Angle Spectroscopic COronagraph, see Brueckner et al. 1995) aboard SOHO (SOlar and Heliospheric Observatory, see Domingo et al. 1995), or COR2 (Howard et al. 2008) aboard STEREO (Solar-TErrestrial RElations Observatory, see Kaiser et al. 2008), with the field of view typically starting around 2.5 $R_\odot$. Between the typical fields of view of EUV imagers and externally occulted coronagraphs, there is generally a gap where the observations are difficult[2]. Historically, this gap has been filled with ground-based coronagraphs, observing the emission line corona in visible or near-infrared (Altrock 2004; Tomczyk et al. 2008) or observing white light (Fisher et al. 1981; de Wijn et al. 2012; St. Cyr et al. 2015), but these are limited to daytime good-weather viewing and in the case of white light, to observing in polarized brightness (since the background sky brightness is largely unpolarized).

One may try to fill in the gap by expanding fields of view of EUV imagers using occultations (Slemzin et al. 2008; Rochus et al. 2020; Auchère et al. 2023a) or off-points away from the

Sun (Tadikonda et al. 2019; Seaton et al. 2021). However, solar EUV emission is proportional to the integral of the square of the coronal electron density (n_e^2) along the line of sight. As the coronal density rapidly decreases with height, the signal-to-noise ratio quickly decreases, so the required exposure times become long (e. g. 1000 s). This may lead to the smearing of propagating structures, which complicates studies of dynamic phenomena (Auchère et al. 2023a).

The coronal white-light emission is proportional to the line-of-sight integral of n_e. It therefore decreases with height slower than the EUV emission, so observing the corona in white light may allow faster imaging with at least comparable signal-to-noise ratio. Such observations can be made with internally occulted coronagraphs, which generally have a field of view starting at lower heights than externally occulted coronagraphs. For example, the field of view of the LASCO C1 (Brueckner et al. 1995) and SECCHI COR1 (Howard et al. 2008) coronagraphs start at 1.1 $R_\odot$ and 1.4 $R_\odot$ respectively. However, internally occulted coronagraphs allow light from the full solar disk to enter through their entrance apertures, which generally leads to high straylight levels on the detector.

Straylight in coronagraphs is very difficult to suppress when corona below 2.5 $R_\odot$ is observed. High levels of straylight mean that the signal-to-noise ratio, the contrast of small-scale features, and the effective spatial resolution become low. Total solar eclipse observations do not suffer from straylight issues, but they are rare and last only for a short time.

In this paper, we report the scientific objectives and instrument design of the ASPIICS coronagraph (Association of Spacecraft for Polarimetric and Imaging Investigation of the Corona of the Sun) that was launched aboard the Proba-3 formation flying mission[3] of the European Space Agency (ESA) on 5 December 2024. ASPIICS is an externally occulted coronagraph designed to image the solar corona between 1.099 $R_\odot$ and 3 $R_\odot$ in white light and in two narrow passbands, thus covering the gap between typical fields of view of EUV imagers and classical externally occulted coronagraphs. In Sect. 2, we describe the general principle of the ASPIICS observations and explain how the straylight is decreased due to the unique formation flying concept. Section 3 provides a description of the scientific objectives of ASPIICS. Sections 4 and 5 report the mission profile and instrument design, respectively. Section 6 summarizes the instrument performances measured during on-ground calibration. Section 7 describes the concept of operations. Section 8 provides a short summary of the instrument and mission perspectives.

2. Mission concept

In externally occulted coronagraphs, the solar disk light diffracted by the external occulter represents the major source of straylight (Koutchmy 1988; Aime 2013; Rougeot et al. 2017, 2018; Shestov & Zhukov 2018; Shestov et al. 2019, 2021; DeForest et al. 2025). According to theoretical calculations by Fort et al. (1978) and Lenskii (1981), the intensity L_{A1} (in relative units) of diffracted light in the center of the entrance aperture can be expressed as follows (we use notations of Bout et al. 2000):

---

[*] Deceased
[1] We do not discuss here the radio imaging of the corona (Gary 2023), which only has a low spatial resolution.
[2] This gap partially overlaps with the middle corona defined by West et al. (2023).

[3] The name of the mission, "Proba", means "Try!" in Latin. An alternative, older variant of spelling, "PROBA" (meaning "PRoject for On-Board Autonomy") was also used for the line of small technology demonstration ESA missions that includes PROBA-1, PROBA2, PROBA-V, and Proba-3. Both variants of the spelling have been used in the past for these missions. In this paper, we adopt the spelling "Proba-3".
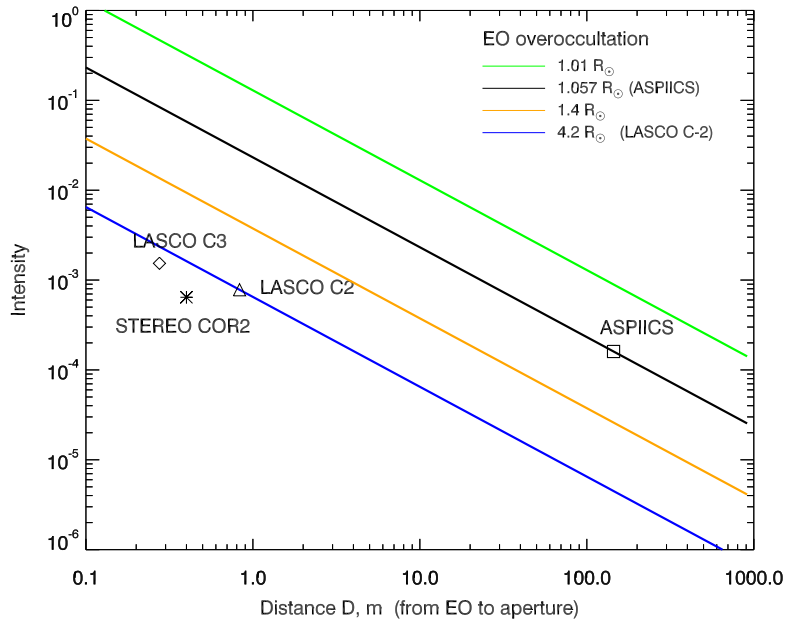
Fig. 1: Light diffracted on the external occulter (EO) of a coronagraph critically depends on the distance D between the EO and the entrance aperture. The plot shows the dependence of the diffracted light intensity at the center of the aperture L_{A1} on D according to Eq. (1) for several angular sizes of the external occulter expressed in solar radii $R_\odot$, shown by slanted lines of different colors. In comparison with other externally occulted coronagraphs, the diffracted light intensity in ASPIICS is lower despite significantly smaller overoccultation.

$$L_{A1} = \left\{ \pi^2 r_\odot \left[1 - \left(\frac{r_\odot D}{R_{EO}} \right)^2 \right] \right\}^{-1} \frac{\lambda}{R_{EO}}, \qquad (1)$$

where $r_\odot$ is the angular radius of the Sun, D is the distance between the external occulter and the entrance aperture, R_{EO} is the radius of the external occulter and λ is the wavelength of observation.

The intensity of the diffracted light for several representative situations is shown in Fig. 1. The slanted lines show the diffracted light intensity for several angular sizes of the external occulter (expressed in $R_\odot$). For a given occultation, the diffracted light intensity decreases with increasing distance D between the external occulter and the entrance aperture. The values for several classical externally occulted coronagraphs are shown in Fig. 1 as well[4]. The LASCO C2, C3, and STEREO COR2 coronagraphs[5] are grouped around $D \sim 1$ m. For these misions, increasing D beyond this value would be impractical due to considerations of the spacecraft size (of the order of a couple of meters for SOHO). This explains the use of internally occulted coronagraphs such as LASCO C1 and COR1 for observations of the inner corona from SOHO and STEREO, respectively.

Due to the unique Proba-3 concept of two spacecraft flying in formation (see Sect. 4), the distance $D \approx 144$ m for ASPIICS, representing an increase by two orders of magnitude in comparison with classical coronagraphs. This allows us to achieve, in the

same time, a better occultation (1.057 and 4.2 $R_\odot$ for ASPIICS and LASCO C2, respectively) and a more efficient rejection of diffracted light (by a factor 3–10). This demonstrates a unique advantage of ASPIICS.

The main observations by ASPIICS will be the coronal imaging in white light (wide spectral passband, 5363–5658 Å) between 1.099 and 3 $R_\odot$ (see Fig. 2), thus allowing for a significant overlap with the low corona observations by EUV imagers (e.g. SDO/AIA up to 1.27 $R_\odot$, see Lemen et al. 2012), and high corona observations by classical externally occulted coronagraphs (e.g. SOHO/LASCO C2 from 2.2 $R_\odot$, see Brueckner et al. 1995). In addition to the total brightness images, polarized brightness images of the corona will be taken with the same spectral filter. Polarized brightness data allow us to determine the coronal density more reliably than unpolarized data (e.g. Koutchmy et al. 1977; Decraemer et al. 2019; Lamy et al. 2020; Edwards et al. 2023). Two filters with narrow spectral passbands will be used, centered on the coronal green line (Fe XIV, 5304 Å in vacuum) showing emission of the corona at temperatures around 2 MK (e.g. Schwenn et al. 1997; Kim 1997; Mierla et al. 2008; Ramesh et al. 2024), and the He I D_3 line at 5877 Å showing emission of prominences at temperatures around 0.01 MK (e.g. Jejčič et al. 2018). The images will be projected on the square detector with 2048×2048 pixels, with each pixel corresponding to 2.817″. The nominal synoptic cadence will be 1 minute, although observations using a quarter of the field of view allow for higher cadences (up to 2 s).

3. Scientific objectives

The Proba-3/ASPIICS coronagraph will examine the structure and dynamics of the corona in the crucial region between 1.1

---

[4] We note that Eq. (1) is valid for a single occulter, and modern coronagraphs (LASCO C2 and C3, and COR2) have triple disk occulters. Eq. (1) is used here to illustrate the physical principle of diffracted light calculation.

[5] The Metis coronagraph (Antonucci et al. 2020) has an inverted external occulter, which cannot be described by Eq. (1).
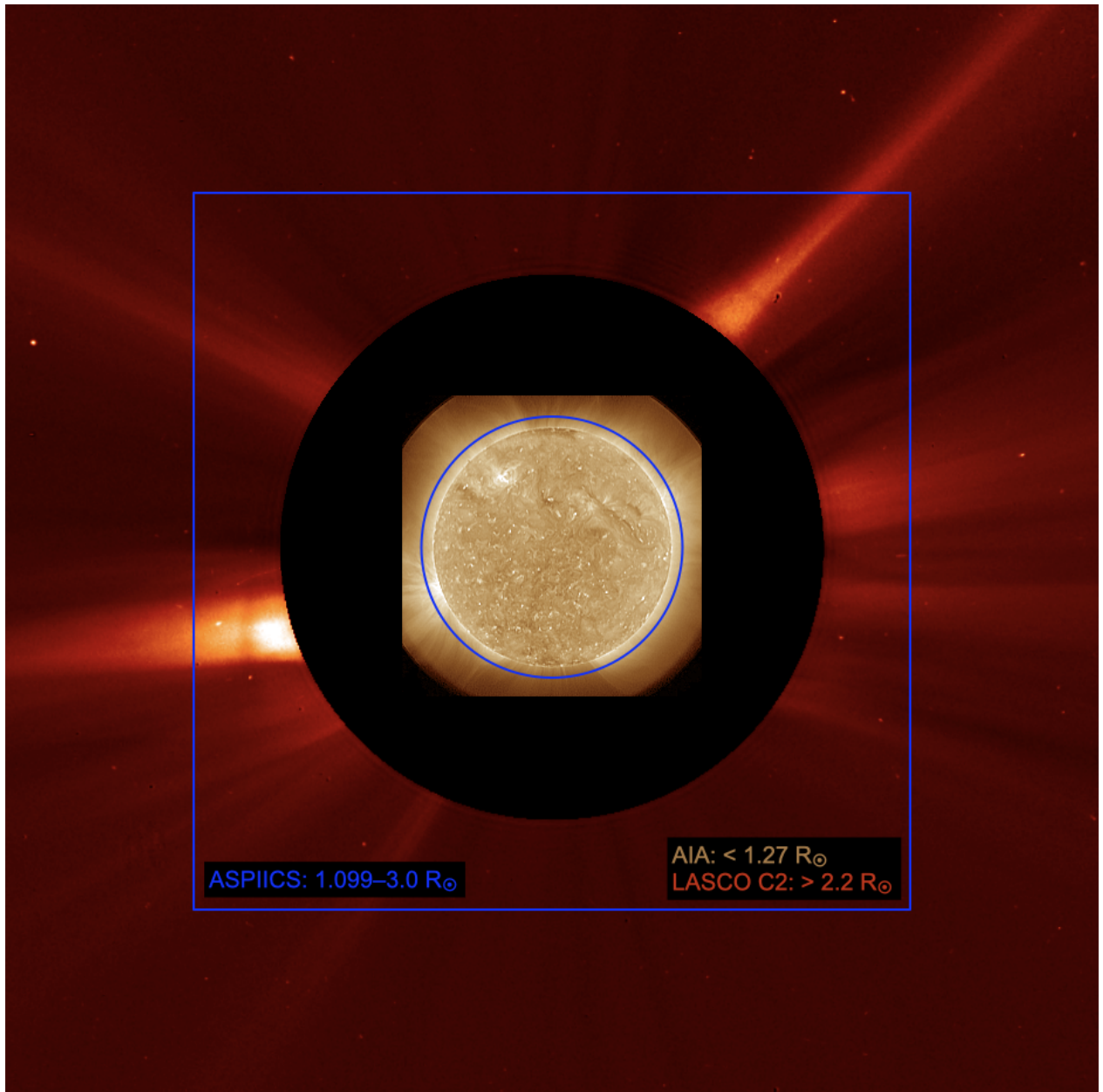
Fig. 2: Observations of the solar corona by classical externally occulted coronagraphs (SOHO/LASCO C2 image shown in red) and EUV imagers (SDO/AIA image shown in brown) leave an important gap where observations are difficult. The field of view of the ASPIICS coronagraph aboard the Proba-3 mission is shown in blue.

and 3 $R_\odot$, which is difficult to observe (Fig. 2). The top-level scientific objectives of ASPIICS are:

1. Understanding the physical processes that govern the quiescent solar corona, by answering the following questions:
   - What is the nature of the solar corona on different scales?
   - What processes contribute to the heating of the corona?
   - What processes contribute to the solar wind acceleration?
2. Understanding the physical processes that lead to CMEs and determine space weather, by answering the following questions:
   - What is the nature of the structures that form the CME?
   - How do CMEs erupt and accelerate in the low corona?
   - What is the connection between CMEs and active processes close to the solar surface?

- Where and how can a CME drive a shock in the low corona?

In the following sections, we describe each of the science objectives.

3.1. Understanding the physical processes that govern the quiescent solar corona

3.1.1. What is the nature of the solar corona on different scales?

The large-scale structure of the solar corona is dominated by magnetically open dark coronal holes and bright streamers extending from closed coronal loops. During the years of low solar activity, a large coronal hole is situated around each pole, and

helmet streamers constitute the streamer belt at low latitudes. During the epoch of high activity, polar coronal holes disappear and the corona is dominated by streamers all around the solar disk (e.g. Loucif & Koutchmy 1989).

Due to the low-beta environment of the corona near the surface (Gary 2001; Rodríguez-Gómez et al. 2024), the plasma structure of the corona strongly depends on the configuration of the coronal magnetic field. Observations and models demonstrate that the magnetic configuration of the streamer helmet may consist of one (Saito & Hyder 1968; Koutchmy 1971; Pneuman & Kopp 1971), two (Saito & Tandberg-Hanssen 1973; Wang et al. 2007; Rachmeler et al. 2014) or three (Schwenn et al. 1997; Noci et al. 1997; Banaszkiewicz et al. 1998; Wiegelmann et al. 2000) loop arcades. The arcades are situated below the bright quasi-radial streamer stalk, which represents the plasma sheet centered around the neutral current sheet (for one or three arcades) or around a separatrix surface between magnetic fields of the same polarity (for two arcades – so-called pseudostreamer).

However, the coronal magnetic field is currently difficult to measure (see e.g. reviews by Landi Degl'Innocenti & Landolfi 2004; Trujillo Bueno 2010). The global coronal magnetic field is now routinely extrapolated from photospheric magnetograms using models such as the potential field source surface (PFSS) model (Schatten et al. 1969; Hoeksema et al. 1983), and magnetohydrodynamic (MHD) models (Linker et al. 1999; Yeates et al. 2008; Lionello et al. 2009; Downs et al. 2025). The models do provide important information about the structure of the coronal magnetic field (e.g. Wang et al. 2000b): the positions of coronal holes (and of the heliospheric current sheet at 1 au) can be well derived from these models. However, determining the structure of streamers in this way may still be challenging (Wang et al. 2002; Saez et al. 2005; Zhukov et al. 2008). Even for the low solar activity epoch, the coronal field extrapolated from surface measurements is clearly model-dependent (Yeates et al. 2010; Wiegelmann et al. 2017). The extrapolated field is generally static and cannot account for slow evolution of streamer structure. Quite often, extrapolations fail to reproduce accurately complex topologies and dynamics inferred from remote-sensing observations of coronal structures, especially during high solar activity (e.g. Zhukov et al. 2008; Benavitz et al. 2024).

The crucial transition between closed-field regions of the low corona (magnetic field dominated) and open-field regions higher up (solar wind dominated) is poorly observed by modern space missions (see e.g. West et al. 2023). Magnetic field topology can be inferred using observations of coronal structures (Jones et al. 2016; Bemporad 2023; Shi et al. 2024). Proba-3/ASPIICS will be well suited to provide crucial seamless observations of the low corona up to 3 $R_\odot$ in white light. It will track the connectivity of coronal structures to the solar surface and, in combination with state-of-the-art MHD models (Mikić et al. 2018; Downs et al. 2025), will allow us to determine reliably the coronal magnetic field configuration.

On smaller scales, the solar atmosphere appears extremely structured and dynamic, in particular when observed at the best available spatial resolution (e.g. Koutchmy et al. 1994; November & Koutchmy 1996; Delannee et al. 1998; Feldman et al. 1999; Zhukov et al. 2000; Cirtain et al. 2013; Berghmans et al. 2021). The fine structure appears down to the limit of the spatial resolution of the instruments. Therefore, it is likely that the elementary structures have not yet been fully resolved. The spatiotemporal fine-structuring of plasma and magnetic field in the solar atmosphere determines the dissipation of energy and the fundamental physical processes leading to plasma heating, cooling, radiation, motion, and wave generation, and to solar wind

and energetic particle acceleration. These processes, in turn, influence the fine structure of the corona. The dominant spatial and temporal scales of energy build-up, storage, and dissipation are presently unknown.

ASPIICS will help answering the question about solar corona structuring and dynamics on different scales. Using its white-light and polarization brightness observations, ASPIICS will be able to resolve density structures down to 5.63″ spatial resolution (4100 km, two pixels). This is largely superior to the resolution of other space coronagraphs like LASCO C2 (22.8″). Only Solar Orbiter/Metis will reach the same linear spatial resolution, but only during a short time close to Solar Orbiter perihelia (Antonucci et al. 2020). The high resolution of ASPIICS will be available seamlessly from low to high solar corona (1.17– 3 $R_\odot$), outside of the narrow vignetting zone (see Sect. 5.1.1). Sophisticated image processing algorithms (e.g. Stenborg & Cobelli 2003; Morgan et al. 2006; Druckmüller et al. 2014; Auchère et al. 2023b) will be used to improve the image quality further by increasing the contrast of coronal structures. Coronal density structure will be inferred using the polarized brightness inversions (e.g. Lamy et al. 2020) and tomography (Asensio Ramos 2023; Vásquez et al. 2024; Wang et al. 2025). The magnetic configuration of the low corona will be inferred in its crucial region and compared with models (Downs et al. 2025). The excellent spatio-temporal resolution of ASPIICS will allow us to investigate the fine structure and dynamics of the corona above the field of view of modern EUV imagers.

3.1.2. What processes contribute to the heating of the corona?

The coronal heating problem is still one of the most debated questions in solar physics (e.g. Parker 1988; Klimchuk 2006). The consensus is that the coronal heating should be magnetic, i.e. it should occur by continuously extracting free magnetic energy from the dynamic corona. Wave theories of coronal heating consider dissipation of MHD waves launched by turbulent motions in the low atmosphere and propagating upwards (e.g. Davila 1987; Van Doorsselaere et al. 2007). ASPIICS, with its unprecedentedly high cadence (down to 2 s in white light), will be very well suited to measure the wave properties in the corona and their contribution to the coronal heating.

It is well accepted that photospheric magnetoconvection and magnetic field reconnection in the chromospheric network are likely candidates to excite MHD waves that are truly pervasive in the solar atmosphere. Due to a poor knowledge of local plasma and magnetic field parameters, it is difficult to determine if these waves can be efficiently dissipated to heat the corona. Another important problem is how much of the wave energy flux generated in the lower atmosphere can propagate to the corona (and not e.g. be reflected at the transition region interface).

Recent observational efforts concentrated on the detection of Alfvén waves, which are theoretically considered to be the best able to transport the energy from the chromosphere to the corona. The wave flux in the chromosphere was estimated to be large enough to satisfy the coronal heating energy requirements (De Pontieu et al. 2007; Jess et al. 2009). Estimates of the Alfvén wave flux in the corona are more controversial, with perhaps a large energy flux that might be contained in still unresolved waves (Tomczyk et al. 2007; McIntosh et al. 2011; Bailey et al. 2025; Morton et al. 2025). Unlike linear Alfvén waves, which are non-compressive, non-linear Alfvén waves can drive density fluctuations (Hollweg 1971) that may be detected by ASPIICS due to its unique capabilities (low straylight, large dynamic
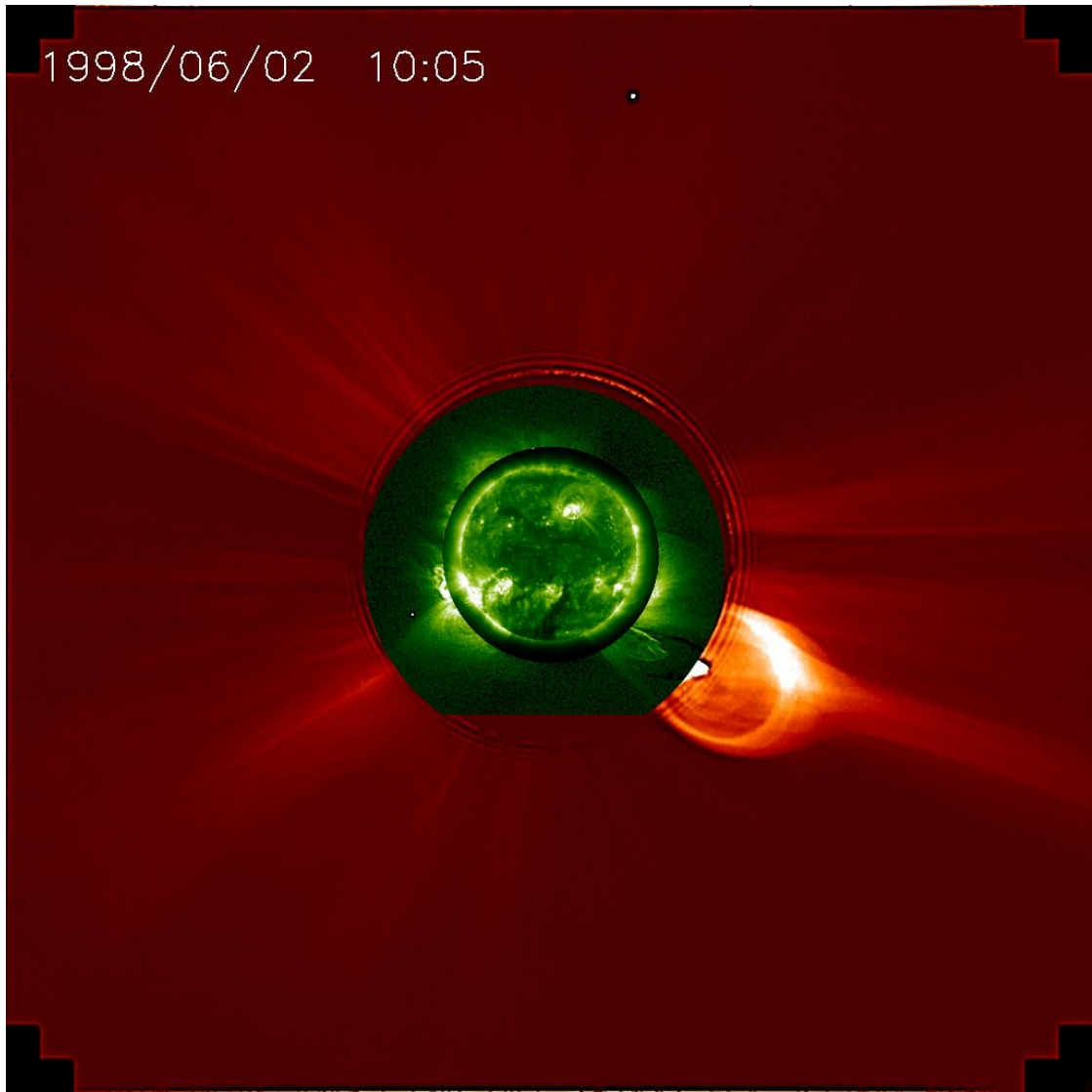
Fig. 3: Coronal mass ejection (CME) imaged by SOHO on 2 June 1998. The innermost image is taken by EIT in the Fe XII passband at 195 Å, the middle image by LASCO C1 in the Fe XIV line at 5304 Å, the outer image by LASCO C2 in white light. Contrast of small-scale structures was increased using the algorithm by Stenborg & Cobelli (2003). Three-part CME structure (evidence of a magnetic flux rope configuration) is well visible. ASPIICS will be able to image for the first time the CME dynamics seamlessly from 1.1 to 3.0 $R_\odot$, and nearly simultaneously in white light, Fe XIV and He I D$_3$ passbands.

range and high signal-to-noise ratio). High spatial and temporal resolution of ASPIICS is perfectly suited to detect coronal waves via observations of quasi-periodic intensity perturbations (e.g. Liu et al. 2011). Complementary observations in the Fe XIV passband and in white light mode will be very important as they will provide constraints on thermal properties of oscillations and waves.

Except for the detection of the Kelvin-Helmholtz instability high in the corona (Feng et al. 2013; Paouris et al. 2024) and CME-associated streamer waves (Feng et al. 2011; Decraemer et al. 2020), observations of coronal waves were up to now made only at rather small radial distances (up to around 1.25 $R_\odot$). AS-PIICS will be able to determine properties of coronal waves in its field of view up to 3 $R_\odot$. Combining electron densities derived from white-light ASPIICS measurements with temperature information obtained from the Fe XIV passband data, one can estimate the wave flux as a function of height over an unprecedented radial range.

Due to novel observations of coronal waves and oscillations, ASPIICS will make an important contribution to the rapidly developing field of coronal seismology (Nakariakov & Verwichte 2005; Banerjee et al. 2007; Tomczyk & McIntosh 2009; West et al. 2011; Feng et al. 2013). Parameters of waves and oscillations (e.g. frequency, amplitude, damping rate, the ratio of the first to the second harmonic) will be measured by ASPIICS with a very high precision, and at radial distances (between 1.099 and 3 $R_\odot$ solar radii) hardly accessible to current seismological studies (Decraemer et al. 2020; Sorokina et al. 2024). These observables can then be interpreted in terms of plasma and magnetic field characteristics. ASPIICS will produce white-light images that will for the first time allow us to look at kink-mode oscillations of coronal structures (not only low coronal loops) from the perspective of density perturbations. ASPIICS seismological diagnostics will complement its density diagnostics. ASPIICS will also image prominences in the He I D$_3$ line, so studies of waves
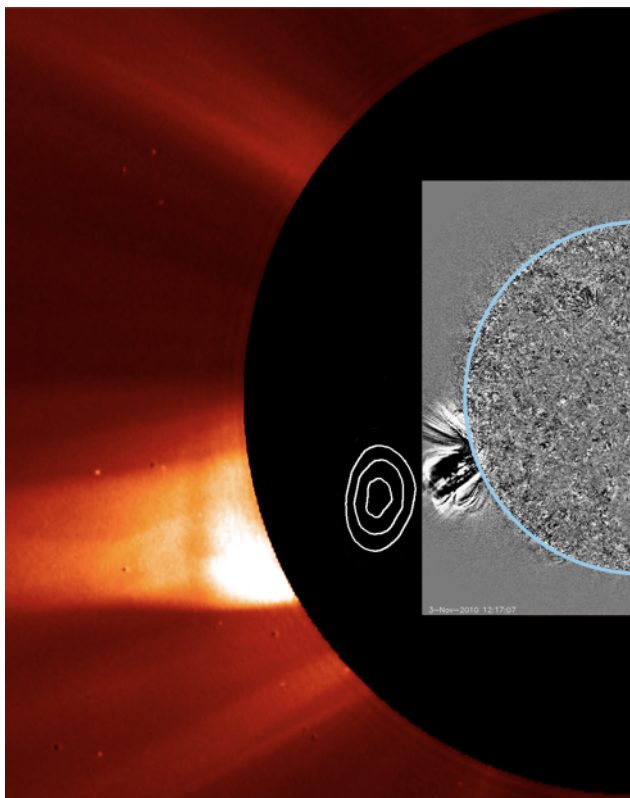
Fig. 4: Low-corona counterpart of a CME (bright front with a dimming inside) observed on 3 November 2010 by SDO/AIA in the 195 Å passband (grey). This is a difference image, with a previous image subtracted to highlight the change of the coronal structure during the CME eruption. The blue circle shows the solar surface (1 $R_\odot$). Nearly simultaneous SOHO/LASCO C2 white light image is shown in red. Isocontours of the emission of a nearly simultaneous type II radio burst imaged by the Nançay Radioheliograph (Kerdraon & Delouis 1997) are shown in the gap between the LASCO C2 and AIA fields of view. This illustrates the lack of coronagraphic observations in the gap region, which will be provided by Proba-3/ASPIICS.

inside of them and prominence seismology will be performed as well (e.g. Okamoto et al. 2007).

3.1.3. What processes contribute to the solar wind acceleration?

Solar wind theory is well developed (Parker 2010; Lemaire 2010), and the overall structure of the heliosphere and its global solar boundary conditions are reasonably well understood from missions such as Helios, Ulysses and SOHO (e.g. McComas et al. 2003). Large coronal holes produce steady streams of fast solar wind, and their plasma originates in the expanding magnetic funnels in coronal holes (Tu et al. 2005). Streams of very variable slow wind originate from the streamer belt (Abbo et al. 2016). However, the details of acceleration processes of individual solar wind streams at the Sun are still unclear.

In particular, the solar sources of the highly variable slow wind streams are the subject of ongoing debate (Abbo et al. 2016; Cliver et al. 2025). The slow solar wind speed was inferred from measurements of the speed of blobs in streamers (Sheeley et al. 1997; Jones & Davila 2009; Lyu et al. 2024; Alzate et al. 2024). It is, however, unclear whether the slow wind orig-

inates from open magnetic field regions with strong expansion factor (in small coronal holes or the outer regions of large coronal holes, see e.g. Wang et al. 2009; Ngampoopun et al. 2025), from the interchange reconnection between open and closed field lines in streamers or pseudostreamers (Wang et al. 2000a; Higginson et al. 2017; Pellegrin-Frachon et al. 2023; Romano et al. 2025), from the edges of streamers and near the streamer cusp (e.g. Gosling et al. 1981; Wang et al. 1998), from active region loop expansion (Uchida et al. 1992), or from open field near active regions (Sakao et al. 2007; Slemzin et al. 2013). Different mechanisms acting in different places at different times is also a possibility, which may explain high variability in the slow wind.

Both coronal holes and streamer belt show a variety of small-scale dynamic events: detachments (Koutchmy & Fagot 1973), blobs (Sheeley et al. 1997; Jones & Davila 2009), inflows (Sheeley & Wang 2007; Wang & Hess 2018), jets (Cirtain et al. 2007; Chitta et al. 2023b), and other density structures (Viall & Vourlidas 2015; DeForest et al. 2018). Some of these phenomena are probably manifestations of interchange reconnection between open and closed field lines in the solar wind source region (Shibata et al. 1992; Pariat et al. 2009; Lynch 2020). The coronal hole boundary region is expected to be a location of magnetic field disruption and reconnection, since many coronal holes rotate quasi-rigidly as compared to the differentially rotating photosphere (e.g. Sime 1986; Wang et al. 1996). A narrow dynamic region around the open-closed field boundary can also be represented as a layer of separatrices and quasi-separatrices (so-called S-Web) that continuously releases solar wind due to interchange reconnection (Antiochos et al. 2011; Baker et al. 2023; Wilkins et al. 2025). This continuous injection of mass and energy may be relevant to the solar wind acceleration (Cirtain et al. 2007; Chitta et al. 2023a), so understanding small-scale dynamics is crucial to solve the solar wind problem.

With ASPIICS, it will be possible to make detailed investigations of small-scale dynamics in the solar wind source region, in particular at the interface between fast and slow streams. Due to its high spatial and temporal resolution in white light, ASPIICS will measure the fine structure and dynamics in unprecedented detail. ASPIICS will look for signatures of interchange reconnection that can provide material for coronal streamers and slow solar wind. Due to its high spatial and temporal resolution, dynamic range and low straylight, ASPIICS will measure the slow solar wind speed continuously up to 3 $R_\odot$, thus providing a missing link between previous measurements (Sheeley et al. 1997; Jones & Davila 2009; Alzate et al. 2024) that are somewhat contradictory. This will help us to solve a long-standing problem of the slow solar wind origin.

Acceleration mechanisms of the fast and slow solar wind will also be probed by observing compressive fluctuations of the coronal brightness. The frequency spectra of intensity fluctuations are indicative of whether or not a turbulent cascade transfers energy to small scales where it can be dissipated to accelerate the solar wind. While magnetic and velocity field fluctuations can be reasonably described in terms of incompressible MHD turbulence, the nature of density fluctuations is still unclear (Bruno & Carbone 2013). The turbulence may already be developed in the corona and may carry the imprint of different sources of fast and slow solar wind streams.

The spectrum of density fluctuations can be obtained from coronagraphic measurements (Bemporad et al. 2008; Telloni et al. 2009, 2024) and compared to spectra obtained in situ. By applying a similar analysis to high-cadence (up to 2 s) time series of the total and polarized white-light emission, ASPIICS will derive unique maps of density fluctuations spectra in both
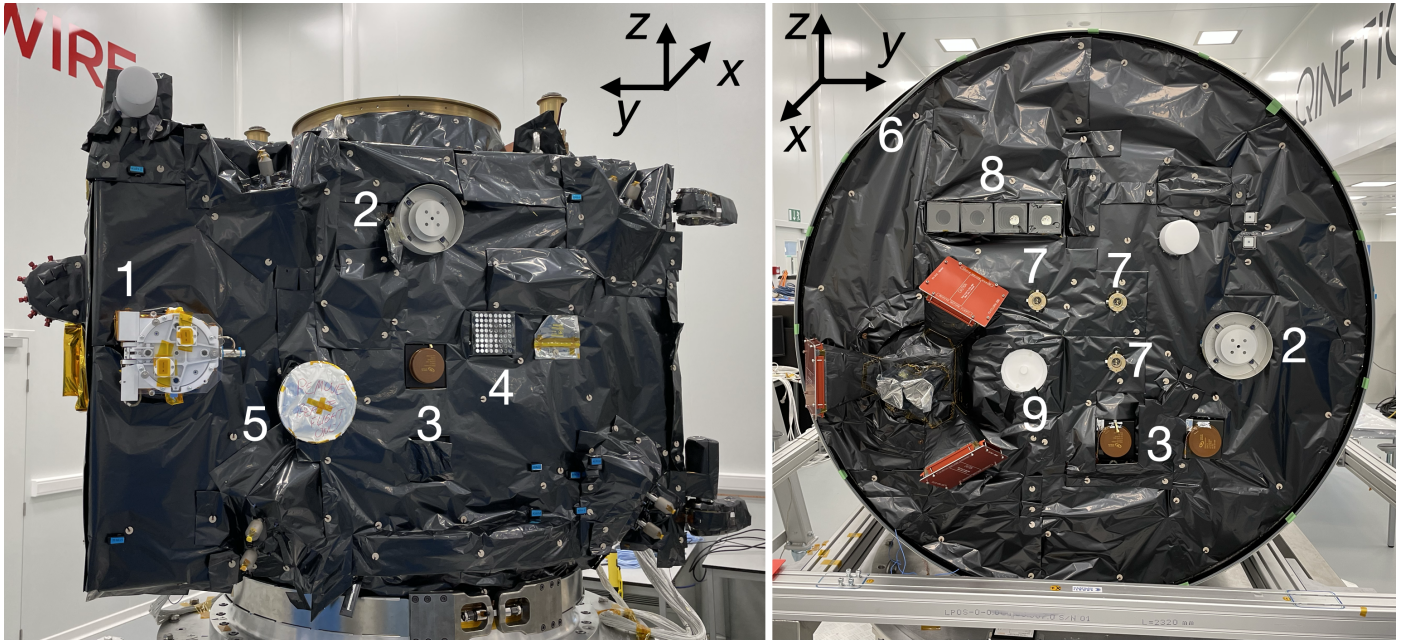
Fig. 5: Two spacecraft of the Proba-3 mission. Left panel: the Coronagraph Spacecraft (CSC). Right panel: the Occulter Spacecraft (OSC). The annotations highlight key subsystems of the mission: the entrance door of the ASPIICS coronagraph (1), GNSS antennas (2), antennas of the Inter-Satellite Link (ISL, 3), some mires of the Visual-Based System (4), Corner Cube Retro-Reflector (5), which is a part of the Fine Lateral and Longitudinal Sensor (FLLS), the edge of the external occulter (6), three LEDs of the Occulter Position Sensor Emitter (OPSE, 7), wide-angle and narrow-angle cameras of the VBS (8), laser of the FLLS (9). The axes of the coordinate systems are shown in each panel, with the x-axis pointing away from the Sun, z-axis pointing towards the ecliptic north, and y-axis complementing the right-handed system. The theoretical formation corresponds to the perfect alignment of the respectively x, y, and z axes attached to the two spacecraft.

fast and slow wind streams simultaneously and close to their source. Spectra of density fluctuations observed by ASPIICS will be compared to models (e.g. Chandran et al. 2009) in order to understand the role of turbulence in the solar wind acceleration process.

3.2. Understanding the physical processes that lead to CMEs

CME initiation and evolution remain major themes in solar physics. Even though many CME initiation models coexist at present, the exact processes that may cause a CME are still unknown. It is now clear that CMEs are related to a restructuring of the coronal magnetic field. The energy of a CME is stored in strongly non-potential field configurations (e.g. Titov & Démoulin 1999) for a long time and then quickly released during an eruption due to a loss of the magnetic field equilibrium (Low 1996; Forbes 2000), or due to an instability (e.g. Kliem & Török 2006).

3.2.1. What is the nature of the structures that form the CME?

In order to understand solar eruptions, knowledge of the state of the corona prior to a CME is essential, but the link of CMEs to underlying magnetic structures is not yet fully clear (e.g. Duan et al. 2024). In white-light images, CMEs often show a three-part structure (Illing & Hundhausen 1986), composed of a bright leading edge followed by a dark void and finally by a bright core associated with the erupting prominence (Fig. 3). The three-part structure represents a two-dimensional projection of a three-dimensional magnetic flux rope (Hundhausen & Low 1994; Low
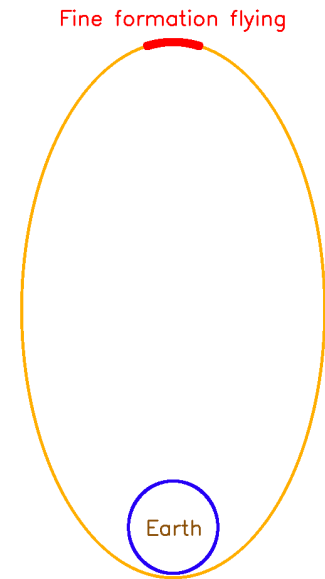

Fig. 6: Scheme of the Proba-3 orbit. The orbital parameters are listed in Table 1.

& Hundhausen 1995; Chen et al. 1997; Thernisien et al. 2009; Song et al. 2023).

The simplest bipolar magnetic configuration of a pre-CME corona that can evolve into a magnetic flux rope is that of a sheared arcade (Priest 1988; Cremades & Bothmer 2004; Titov

et al. 2008). Alternatively, a pre-existing magnetic flux rope may also be present (Canou et al. 2009; Cheng et al. 2013). If the flux rope did not exist before the eruption, it is created by magnetic reconnection once the CME starts (Amari et al. 2011). The flux rope ejection is accompanied by a large-scale magnetic field restructuring (e.g. Roussev et al. 2007; Su et al. 2013). More complicated configurations of the pre-CME magnetic field are possible, e.g. two-arcade pseudo-streamers (Török et al. 2011; Wang & Hess 2023; Wyper et al. 2024; Lynch et al. 2025) or three-arcade quadrupolar fields (Antiochos et al. 1999; Lynch et al. 2008). The basic physics of the loss of equilibrium or of an instability is believed to be the same regardless of the underlying magnetic configuration (e.g. Wu et al. 2005; Kliem & Török 2006; Amari et al. 2007; Roussev et al. 2007).

Prominence material can be aligned along the flux rope axis and thus serves as a marker for the sheared arcade/flux rope configuration. It is isolated from the surrounding hot corona by the prominence – corona transition region (PCTR, Parenti et al. 2012; Gibson 2018). The study of prominences is an important topic in solar physics: their origin, equilibrium, thermodynamic properties, mass loading and eruption are still not completely understood (e.g. Heinzel et al. 2008; Berger et al. 2011). Coronagraphic observations of prominences are of great interest because the surrounding corona can be studied simultaneously. ASPIICS will provide us with high-resolution, high-cadence simultaneous observations of prominences in the He I D$_3$ passband and of the surrounding corona in white light, complemented by the Fe XIV images. The use of the He I D$_3$ line in ASPIICS has the advantage that this line is optically thin. This permits a straightforward evaluation of the prominence mass, as the emission in this line is well correlated with the emission in the H$_\alpha$ line. By accurately evaluating the mass of erupting prominences, ASPIICS will provide us with crucial insight into the problem of the CME mass budget (e.g. Koutchmy et al. 2008). Direct ASPIICS detection of the He I D$_3$ emission in prominences will also help to infer the D$_3$ line polarization from Metis observations (Heinzel et al. 2023).

A cross-section of a sheared arcade can be observed in projection above the limb as a quiescent dark coronal cavity situated at the base of a helmet streamer (Gibson et al. 2006; Jain Jacob & Maurya 2025). Cavities are surrounded by bright streamer material and sometimes contain a prominence in their center (Low 1996; Marqué 2004). As cavities show the locations of a simpler pre-eruptive magnetic configuration (e.g. Bąk-Stęślicka et al. 2013; Rachmeler et al. 2013), understanding their structure and dynamics before and during eruptions is crucial for solving the CME initiation problem (Gibson 2015).

Cavities are typically visible below 1.6 $R_\odot$, so their observations with space coronagraphs are rare. Due to its seamless field of view from 1.099 to 3 $R_\odot$, high cadence and unprecedented straylight rejection, ASPIICS will be an ideal instrument to investigate coronal cavities and their evolution into CMEs. Inversion of ASPIICS polarization brightness measurements will provide densities inside and outside cavities (Fuller & Gibson 2009). The Fe XIV images will be used to characterize the thermal state of the cavity plasma and ambient streamer material. The He I D$_3$ passband will be used to image the morphology and dynamics of the prominence material often found inside the cavity (Heinzel et al. 2008). Properties of cavities, prominences inside of them and ambient streamer material derived by ASPIICS will be analyzed to understand their dynamics and relation to eruptions (Song et al. 2025), as well as the mass balance in the corona and in CMEs.

3.2.2. How do CMEs erupt and accelerate in the low corona?

CMEs appear from magnetic field configurations that have enough of free magnetic energy accumulated during slow evolution of the coronal field in response to photospheric motions. The photospheric motions are too slow to drive most of the CMEs directly. The physics of the energy release process is still not entirely clear (e.g. Emslie et al. 2012). At a certain moment in the evolution of the pre-eruptive magnetic field, an eruption may be triggered, e.g. due to such mechanisms as tether-cutting (Moore et al. 2001), magnetic breakout (Antiochos et al. 1999), kink instability (Fan & Gibson 2003; Török & Kliem 2005), mass loading (Wolfson & Saran 1998; Seaton et al. 2011). This brings the structure to an out-of-equilibrium state (Kliem et al. 2014). Once the force balance is lost, a driver mechanism leads to the fast acceleration and expansion of the CME.
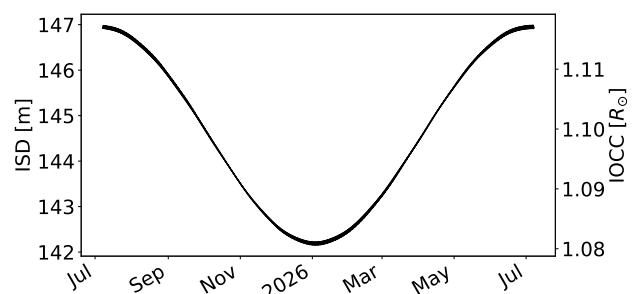

Fig. 7: Variations of the inter-satellite distance (ISD) over the year (left ordinate axis) and the limit of occultation by the internal occulter (position of the 100% vignetting, right ordinate axis). The variations are nearly identical for both quantities, depending mostly on the angular size of the Sun that changes due to the eccentricity of the Earth's orbit. The occultation by the internal occulter fixed inside the telescope does not depend on the ISD.

The driver of CMEs is the magnetic Lorentz force (e.g. Forbes 2000; Zhong et al. 2023). Two main types of driver mechanism are currently envisaged. The first is related to an ideal MHD instability (e.g. Kliem et al. 2014; Filippov 2024). Most probably it is the torus instability, which is due to the hoop force acting on a curved magnetic flux rope (Kliem & Török 2006; Olmedo & Zhang 2010). The torus instability leads to an eruption if the background magnetic field decreases with height quickly enough. The other possible driver mechanism is a resistive mechanism linked to magnetic reconnection under the erupting flux rope (e.g. Lin & Forbes 2000; Karpen et al. 2012; Jiang et al. 2021). The reconnection closes a part of the field overlying the flux rope. This disrupts the force balance and allows the eruption to continue, which leads to new magnetic flux being carried below the flux rope, where it reconnects again (Lin & Forbes 2000). This process thus involves a positive feedback between the flux rope eruption and reconnection underneath. It is still not clear which mechanism is dominant at which circumstances and at which stage of eruption (Zhong et al. 2023; Xing et al. 2024). It is also possible that different mechanisms are acting one after the other or simultaneously. Contributions of different triggering and driving mechanisms are difficult to disentangle.

One of the problems in understanding the CME eruption and evolution in the low corona is that CMEs gain most of their acceleration below 3 $R_\odot$ (MacQueen & Fisher 1983; St. Cyr et al. 1999; Vršnak 2001; Bein et al. 2011), i.e. in a region not very well observed by past and present coronagraphs. CME
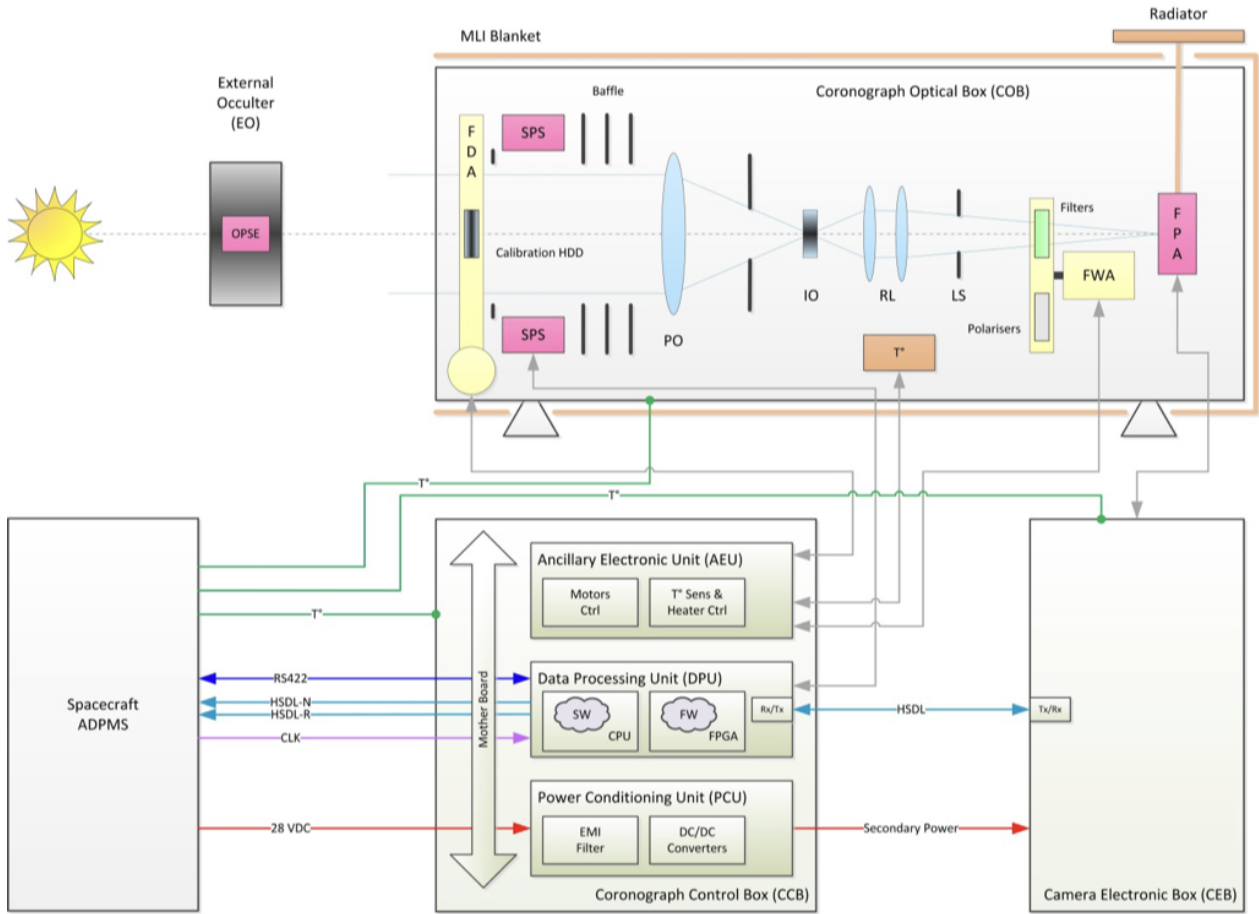
Fig. 8: The block diagram of the ASPIICS instrument.

kinematics is usually measured by three different types of instruments: EUV imagers like SDO/AIA at radial distances $r \lesssim 1.5\ R_\odot$, internally occulted coronagraphs like STEREO/COR1 or SOHO/LASCO C1 at $1.2\ R_\odot \lesssim r \lesssim 2.5\ R_\odot$, and by externally occulted coronagraphs at $r \gtrsim 2.5\ R_\odot$ (Bein et al. 2011). The low cadence of the LASCO C1 data allowed at best having only a handful of measurements during the CME impulsive acceleration (Zhang et al. 2001), and STEREO/COR1 data are subject to significant uncertainties due to high straylight (Temmer et al. 2010). These heterogeneous observations do not allow distinguishing between different proposed mechanisms of the CME initiation. Observations connecting ground-based with space-based coronagraphs have also demonstrated the importance of measuring acceleration from white-light observations of the low corona (St. Cyr et al. 1999; Maričić et al. 2007; Bemporad et al. 2007; Bein et al. 2011). Low straylight and a seamless view of the low corona up to $3\ R_\odot$ provided by ASPIICS will help to obtain a complete overview of the CME onset. ASPIICS high cadence and high spatial resolution are necessary for detailed measurements of the CMEs impulsive acceleration in the low corona, especially for fast CMEs that today are not sufficiently well sampled in the critical range where the bulk of the acceleration occurs (Veronig et al. 2018). Speeds of different eruptive structures (e.g. erupting prominence, CME leading edge, multiple fronts) will be measured to determine any velocity dispersion in CMEs and its relation to the CME initiation mechanism (Majumdar et al. 2024; Shaik et al. 2024; Bemporad et al. 2025).

ASPIICS will also contribute to solving the CME origin problem by observing in detail the restructuring of the large-scale magnetic configuration of the corona during CMEs. Its high cadence will allow precise measurements of timing of different events in its field of view: the start of the slow rise of the flux rope or prominence (Cheng et al. 2020; Xing et al. 2024), the onset of the fast reconnection in the flare current sheet below the erupting flux rope (Jiang et al. 2021), the start of the breakout reconnection above the flux rope (Karpen et al. 2012), and any additional reconnection of the erupting flux rope with other magnetic flux systems (Lynch et al. 2025; Veronig et al. 2025). This will allow disentangling contributions of different physical mechanisms in different phases of the eruption (Xing et al. 2024).

3.2.3. What is the connection between CMEs and active processes close to the solar surface?

ASPIICS observations of the low corona will be an indispensable means to investigate the onset and early evolution of CMEs, and their association with other manifestations of solar activity. The link between CMEs and flares has been investigated since a long time (e.g. Gosling 1993; Harrison 1996). It was demonstrated by Zhang et al. (2001) that the CME impulsive acceleration coincides with the rising phase of the associated soft X-ray flare. This correspondence can be interpreted as evidence of a common cause of flares and CMEs – magnetic energy release (e.g. Emslie et al. 2012). In particular, magnetic reconnection can dimin-

ish the magnetic tension of the arcade overlying an erupting flux rope and, at the same time, provide heating and accelerate energetic particles that produce observed flare signatures (e.g. Zhang & Dere 2006; Temmer et al. 2010). However, the synchronous evolution of the flare rising phase and CME acceleration is observed only in around half of CME-flare events (Maričić et al. 2007). High-cadence observations of ASPIICS will better constrain the CME acceleration curve and provide an important evidence on the association of CMEs with flares.

As mentioned above, the pre-eruption configuration of CMEs is often associated with prominences. An eruptive prominence is often observed as the CME core (e.g Plunkett et al. 2000; Mierla et al. 2022). Some prominence material in the CME core is seen to fall (Wang & Sheeley 2002). This mass loss can contribute to the acceleration of the CME in the framework of mass-loading CME models (e.g. Wolfson & Saran 1998; Seaton et al. 2011). Prominences are also excellent markers of a slow rise of the pre-eruptive structure that can lead to a CME if it passes a certain height threshold (Filippov & Koutchmy 2008). ASPIICS measurements of prominence and CME mass in the crucial range of radial distances (up to 3 $R_\odot$) will be combined with measurements of eruption kinematics. Coronagraphic observations represent the only reliable way to measure the CME speed, so high-cadence ASPIICS observations will be uniquely suited to determine the force balance in CMEs during their acceleration in the low corona.

ASPIICS will provide a new view of such CME-associated dynamic phenomena as coronal dimmings (e.g. Rust & Hildner 1976; Sterling & Hudson 1997; Zhukov & Veselovsky 2007; Veronig et al. 2025) and "EIT waves" (e.g. Thompson et al. 1998; Zhukov 2011; Liu & Ofman 2014). These phenomena are usually observed by EUV imagers. Due to complicated dependence of the EUV line intensity on temperature and density, plasma parameters in dimmings and EIT waves are difficult to evaluate (e.g. Zhukov & Auchère 2004). The unique information on the coronal density derived by ASPIICS will be combined with temperature information inferred from its Fe XIV observations and from SDO/AIA for the coronal plasma diagnostics. Another crucial ASPIICS advantage is its high cadence: radio observations demonstrate that plasma can evolve very rapidly during a CME (e.g. Maia et al. 1999). ASPIICS data will be thus crucial for our understanding of plasma dynamics during the CME onset.

Spectroscopic observations of CMEs by SOHO/UVCS showed the existence of persistent (up to a few days) high-temperature (more than 8 MK) emission in the CME wake (Ciaravella et al. 2002; Raymond et al. 2003; Bemporad et al. 2006). This unusually hot plasma was ascribed to the heating by reconnection in the post-CME current sheet predicted by CME models (see the review by Forbes 2000). In white light images, current sheets generally correspond to bright ray-like structures (see e.g. Ko et al. 2003; Webb et al. 2003; Ding & Zhang 2024), often exhibiting dynamic fine structure, like blobs and plasmoids (Patel et al. 2020).

However, this interpretation leaves several open problems that can be directly addressed by ASPIICS. The thickness of the reconnection layer is expected to be comparable to the ion Larmor radius (of the order of a few meters in the corona). In contrast, the thickness of post-CME radial structures observed both in white-light and EUV emissions is typically of the order of 10^4–10^5 km, and the projection effects are too weak to account for this discrepancy. Another problem is the unexpectedly long duration of post-CME current sheets. Both problems may point at an effective resistivity much larger than even the anomalous

resistivity. It can be achieved in the turbulent current sheet subject to e.g. the tearing mode instability (Lin et al. 2007; van Ballegooijen & Cranmer 2008). Important evidence in favor of this idea was obtained in UV observations (Bemporad 2008; Susino et al. 2013), although the hard X-ray data indicate the possibility of plasma supply from a hot long-lived source (Saint-Hilaire et al. 2009).

ASPIICS will provide unique observations of post-CME current sheets due to its combination of a large field of view (including the whole region where these current sheets form and evolve), high spatial resolution, and cadence. ASPIICS will allow us to measure the current sheet plasma densities (polarization brightness measurements) and to derive at the same time information on temperature (from Fe XIV images) at different altitudes along the current sheet during its whole lifetime. A deeper knowledge on post-CME current sheets provided by ASPIICS will be of significant importance for our understanding of the fundamental process of magnetic reconnection in astrophysical conditions.

3.2.4. Where and how can a CME drive a shock in the low corona?

Generation of large-scale shock waves in the solar corona, their propagation to the interplanetary space and possibility of energetic particle acceleration by them are major questions in the science of solar-terrestrial relations (space weather, see e.g. Schwenn 2006). Two physical explanations are proposed for the generation of a coronal shock: a flare blast wave and a piston-driven shock due to a CME (Vršnak & Cliver 2008). It is generally accepted that non-corotating interplanetary shock waves are CME-driven (e.g. Schwenn 2006), but the origin of coronal shocks is still a matter of debate. Both CME and flare origins seem to be possible (e.g. Wagner & MacQueen 1983; Cliver et al. 1999; Gopalswamy et al. 2009; Magdalenić et al. 2010, 2012; Jarry et al. 2023).

Observing shock waves by a coronagraph is a complex task due to often-insufficient sensitivity of the instrument and to the difficulty in associating features observed in white light with shocks. White-light shocks are believed to appear as weak bright fronts, typically ahead of some fast CMEs (MacQueen & Fisher 1983; Sheeley et al. 2000; Eselevich & Eselevich 2008; Ontiveros & Vourlidas 2009; Lu et al. 2017) . Another important shock signature is streamer deflection (Sime & Hundhausen 1987; Sheeley et al. 2000; Decraemer et al. 2020). In both cases, however, it is not clear if the wave is a true shock as plasma and magnetic field parameters in the CME and in the ambient corona are poorly known (e.g. Frassati et al. 2024). Vourlidas et al. (2003) used an MHD simulation to confirm that the density enhancement in front of a CME indeed represents a fast-mode shock. They, however, could not observe it below 2.2 $R_\odot$, so it was impossible to determine the moment of the shock formation. Apart from visual inspection of white-light images, CME-driven shocks can be identified in the SOHO/UVCS data with the appearance of broad profiles of the O VI line (Ciaravella et al. 2005). Halo CME fronts were found to correspond to coronal plasma swept up by a shock or a compression wave (Ciaravella et al. 2006; Vourlidas et al. 2013).

Shocks in the low corona can also be detected by observing type II radio bursts in solar dynamic radio spectra (e.g. Cliver et al. 1999). Radio imaging demonstrates that type II bursts first appear very low in the corona (1.2–1.5 $R_\odot$), see e.g. Vršnak et al. (2005); Carley et al. (2013). In addition to the problem of choosing a coronal density model to estimate the shock speed from the

drift rate of type II bursts, the lack of coronagraphic CME observations in this range of radial distances (see Fig. 4) strongly impedes our efforts to solve the problem of the origin of coronal shocks (Magdalenić et al. 2010). STEREO/COR1 observations between 1.1 and 4 $R_\odot$ provided us with an important insight (Gopalswamy et al. 2009), but the lack of concurrent radio imaging observations from the same vantage point is a strong limitation of such studies.

ASPIICS will provide us with important evidence on the origin of coronal shocks due to its unprecedented observations of the region below 3 $R_\odot$, where many shocks originate. High cadence white-light ASPIICS observations, in combination with high-cadence ground-based radio spectra and images of type II bursts, will allow us to understand the shock formation in the low corona. Polarization brightness and white-light observations by ASPIICS will also be used to derive better density models that are crucial to determine the shock speed from type II burst observations in dynamic spectra.

4. Mission profile

The first attempt to observe solar corona from space using formation flying was made in 1975 during the Apollo-Soyuz Test Project mission by the United States and Soviet Union. A camera mounted aboard the Soyuz spacecraft was used to take photos of the corona, while the solar disk was occulted by the Apollo spacecraft. The F-corona was detected (Nikolskiy et al. 1977).

Proba-3 was launched on 5 December 2024 aboard the PSLV-XL rocket (Polar Satellite Launch Vehicle) from Satish Dhawan Space Centre, the main spaceport of the Indian Space Research Organization (ISRO) located in Sriharikota, India. The mission duration is planned to be two years, including four months of the commissioning. Proba-3 consists of two spacecraft (Fig. 5): the coronagraph spacecraft (CSC) and the occulter spacecraft (OSC), see e.g. Llorente et al. (2013) and Peters et al. (2014). The CSC carries the ASPIICS telescope and the OSC carries the circular external occulter disk with a toroid edge. The spacecraft are placed in a highly elliptical orbit (HEO[6]) around the Earth (Fig. 6). The basic parameters of the orbit are listed in Table 1. The orbital period is 19 hours 38 minutes, and during 6 hours centered around the apogee, the two spacecraft will perform precise formation flying, allowing the entrance aperture of ASPIICS to be placed in the shadow created by the external occulter. The inter-satellite distance (ISD) is around 144 m, varying with the change of the Sun-Earth distance during a year as follows:

$$D = \frac{R_{EO} - R_{A1}}{\tan(Cr_\odot)} - \frac{T}{2} - R_c \sin r_\odot, \qquad (2)$$

where $R_{EO} = 0.71088$ m is the radius of the external occulter, $R_{A1} = 0.025$ m is the radius of the entrance aperture, $C = 1.02$ is the occultation factor by the external occulter (edge of the 100% vignetting), $r_\odot$ is the apparent radius of the Sun, $T = 0.035$ m is the thickness of the external occulter disk, $R_c = 0.7$ m is the radius of curvature of the toroid edge of the occulter disk. Figure 7 shows the change of the ISD during the year, which is primarily produced by the change of the apparent radius of the Sun $r_\odot$ due to eccentricity of the Earth's orbit.

---

[6] This acronym can be also expanded to Highly Eccentric Orbit, which is perhaps more precise.

The precision of the alignment of the spacecraft in the longitudinal and lateral directions is around 10 mm and 1 mm, respectively. The radius of the geometric umbra in this configuration is 39.6 mm.

Table 1: Parameters of the Proba-3 orbit at the beginning of the mission

Parameter name	Parameter value
Perigee height	600 km
Apogee height	60530 km
Semi-major axis	36942.96 km
Eccentricity	0.8111
Inclination	59°
RAAN[a]	142°–148.1°
Argument of perigee	188°
Orbital period	19 h 38 min

[a] Right ascension of the ascending node.

To maintain the two spacecraft in formation, a number of technologies are used. First of all, the positions and velocities of the two spacecraft are refined using relative GNSS (Global Navigation Satellite System) when the spacecraft pass near the orbital perigee (Ardaens et al. 2013). After the GNSS visibility is lost, this information is propagated further in time, up to the availability of the data from the Visual-Based System (VBS) mounted on the OSC. The VBS consists of a Wide Angle Camera (WAC) and a Narrow Angle Camera (NAC), which are used to detect nine blinking mires (LEDs) on the CSC and thus image the CSC directly during flight. The Fine Lateral and Longitudinal Sensor (FLLS, see Bradshaw et al. 2018) includes a beam produced by an infrared laser (working wavelength 980 nm) mounted on the OSC. The laser beam is reflected by the CCRR (Corner Cube Retro-Reflector) placed on the sun-facing side of the CSC. The reflected laser beam is captured by the optical head unit of the FLLS for precise lateral and longitudinal measurement of the CSC position with respect to the OSC. Adjustment of position is performed, if necessary, using thrusters. The Inter-Satellite Link (ISL) is a radio communication means used by the two spacecraft to exchange information and coordinate their maneuvers.

The formation flying will be maintained autonomously over 6 hours in every orbit. This corresponds to around a factor 100 improvement in the duration of uninterrupted observations in comparison with a total eclipse observed on the ground (maximum 7 minutes 40 seconds). The baseline total observation time is determined by the available fuel and is currently estimated to constitute 1000 hours over the 20-month duration of the nominal mission. On average, Proba-3 will observe the corona more than two orbits per week, which constitutes around a factor of 50 improvement in the occurrence rate in comparison with a total eclipse (at most once per year, rarely twice a year).

Five ground stations (in Spain, Chile, Australia, and French Guyana) will be used to downlink the science, housekeeping, and ancillary data.

5. Instrument design

Early works on instrument design were reported by Lamy et al. (2007), Lamy et al. (2010), and Vives et al. (2010), and the evolution towards the final design was described by Renotte et al.
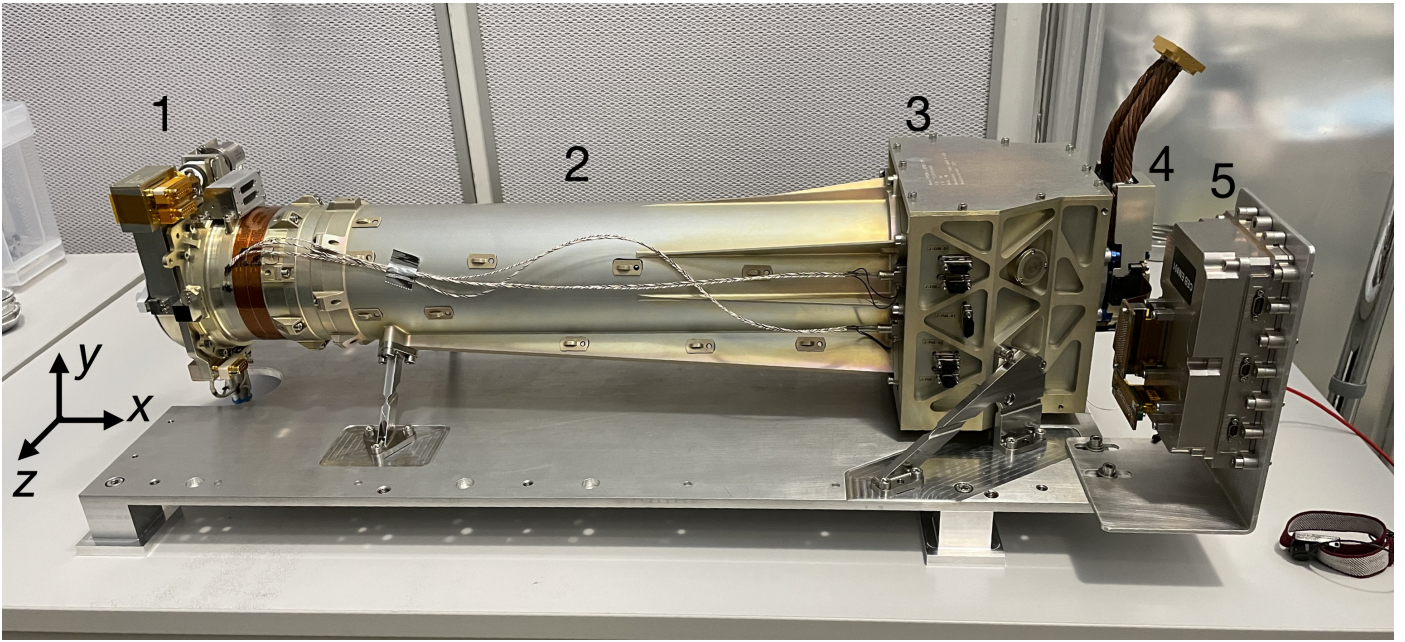
Fig. 9: A photo of the ASPIICS telescope. The annotations highlight key subsystems of the instrument: front door assembly (FDA, 1), telescope tube (2) carrying the lenses, equipment box (EQB, 3) that supports the filter wheel inside of it and the focal plane assembly (FPA, 4) outside of it, Camera Electronics Box (CEB, 5). The axes of the coordinate system attached to the instrument are shown, with the *x*-axis parallel to the optical axis of the telescope, *y*-axis directed from the bottom of the detector (row 0) to the top of the detector (row 2013), and the *z*-axis complementing the right-handed system. The ideal formation corresponds to the perfect alignment of the respectively *x*, *y*, and *z* axes attached to the telescope and the two spacecraft (see Fig. 5).

(2014) and Galano et al. (2018). The ASPIICS block diagram is shown in Fig. 8, and a photo of the flight model of ASPIICS is shown in Fig. 9. The external occulter mounted on the OSC provides the shadow for the entrance aperture of the telescope placed on the CSC. The entrance aperture is protected by a reclosable door (Front Door Assembly, FDA) that is open during observations. The instrument optics project the image of the corona on the APS (Active Pixel Sensor) detector that has 2048×2048 pixels of 10 μm size. The temperature of the detector is controlled by the radiator that evacuates the excessive heat to an open space. The detector output is read by the Camera Electronic Box (CEB) that transfers the data further to the Coronagraph Control Box (CCB, see Fig. 10). The CCB provides the power to the coronagraph and controls the CEB, the FDA, and the Filter Wheel Assembly (FWA). It also sends the data to the spacecraft computer (Advanced Data and Power Management System, ADPMS), from where they are downlinked to the ground.

5.1. Optical design

ASPIICS is a classic externally occulted Lyot coronagraph. The external occulter is a disk made of CFRP (Carbon Fiber Reinforced Polymer) with the radius R_{EO} = 0.71088 m mounted on the OSC spacecraft. The disk has a toroid edge, which keeps the apparent occulting disk radius constant in the event of a small (up to 1°) tilt of the disk due to possible fluctuations of the pointing of the spacecraft. Another reason for implementing a toroid edge is the reduction of diffracted light by around a factor of 2 compared to a knife edge occulter (Landini et al. 2011).

The optical design of the ASPIICS telescope has been described in detail by Galy et al. (2015). The optical scheme of ASPIICS is shown in Fig. 11. The entrance pupil diameter is

50 mm. Internal baffles are placed between the entrance aperture and the primary objective (PO). The corona is imaged on the detector by a set of successive lenses: O1 (primary objective), O2 (field lens), and O3 (relay lense system). The calculated focal length of the telescope is 734.6 mm.

Diffraction on the external occulter is the main source of straylight in externally occulted coronagraphs (Bout et al. 2000; Aime 2013; Rougeot et al. 2017; Shestov et al. 2019). To suppress it, the image of the external occulter diffraction ring is projected by the primary objective O1 on its conjugate optical plane, where the diffraction ring is blocked by the internal occulter with the outer radius of 1.752 mm. This plane is located on the surface of the O2 field lens, and the internal occulter is slightly oversized compared to the image of the external occulter to cover the diffraction ring fully. The field lens O2 creates an image of the entrance pupil in its conjugate plane, where a circular diaphragm (the Lyot stop) is placed to block the light diffracted by the entrance pupil. The diameter of the Lyot stop is 13.85 mm, which is around 97% of the diameter of the entrance pupil. This optical scheme has been proven successful by previous externally occulted coronagraphs, such as LASCO C2 and STEREO COR2.

5.1.1. Field of view and vignetting

There are two types of vignetting in ASPIICS: due to external and internal occulters (narrow annular zone close to the solar limb), and due to the barrels of the spectral filters (seen at the corners of the image).

For the majority of the previous externally occulted coronagraphs, the whole field of view is partially vignetted by the external occulter, resulting in loss of optical throughput and degradation of spatial resolution. In ASPIICS, due to the large distance
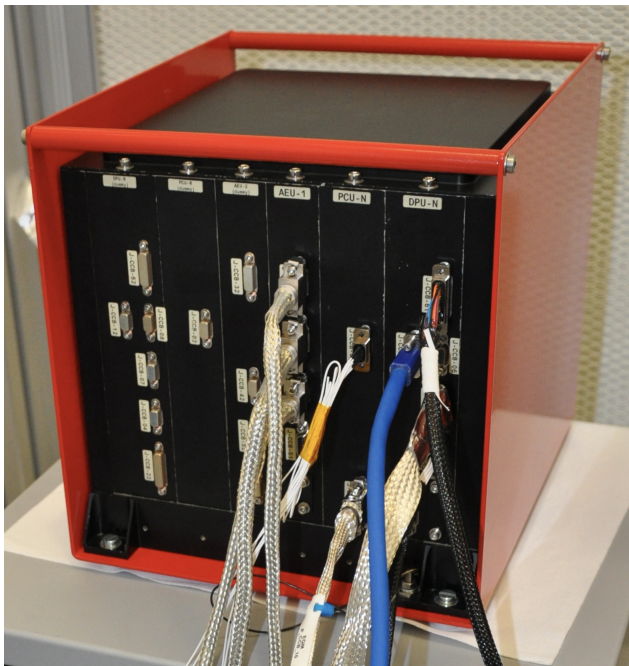
Fig. 10: A photo of the ASPIICS Coronagraph Control Box (CCB), the instrument computer.

between the external occulter and the entrance pupil, the external occulter vignettes only a very narrow ($\sim$ 25 pixels-wide) annular zone around the solar limb. The top panel of Fig. 12 shows the theoretical one-dimensional vignetting function of ASPIICS compared to the vignetting functions of other coronagraphs. As the internal and external occulters are situated in conjugated optical planes of the primary objective, the vignetting is determined by the size of the internal occulter (Shestov et al. 2021). For r_{IO} = 1.752 mm, the field of view is unvignetted above 1.174 $R_\odot$, and below 1.099 $R_\odot$ the field of view is fully vignetted[7]. The ASPIICS vignetting profile is close to that of the Moon. Due to the eccentricity of the Earth's orbit, the apparent size of the Sun changes in the course of the year. With the size of the internal occulter being fixed, this means that the boundaries of the vignetting zone slightly change too, see Fig. 7. At the closest approach to the Sun, the vignetting zone starts at 1.081 $R_\odot$, and at the furthest approach it starts at 1.117 $R_\odot$. We emphasize that even if the variation of the edge of the vignetting zone is similar to the change of the ISD (see Fig. 7), the vignetting zone variation is not produced by the ISD change but only by the change of the apparent size of the Sun.

A consequence of the vignetting profile is that the spatial resolution of ASPIICS is pixel-limited in most of the field of view (Fig. 12). The detector pixel size is 2.817″, which gives the two-pixel spatial resolution of 5.634″. The linear spatial resolution is 4085 km. In the vignetted zone, the spatial resolution is diffraction-limited and rapidly degrades near the fully vignetted zone (Theys et al. 2022).

ASPIICS has higher angular resolution than LASCO C2 and C3, Metis, and COR2 coronagraphs (Fig. 12, bottom panel). However, it should be noted that the linear pixel-limited spatial resolution of the Metis coronagraph near the Solar Orbiter peri-

helion of 0.28 au (around 4300 km, two pixels) is very similar to that of ASPIICS.

Barrels of the ASPIICS spectral filters produce vignetting in the image corners starting at $\sim$ 1° (i.e. at distances above 3.75 $R_\odot$ from the solar center; see Fig. 13). Thus, the field of view of ASPIICS has a complex shape, mainly determined by the square detector with linear scale 1.6° (from −3 to 3 $R_\odot$), the minimal height of the unvignetted zone of 1.174 $R_\odot$ determined by the internal occulter, and the maximal height of 3.75 $R_\odot$ near the corners of the image.

5.1.2. Filters and polarizers

The filter wheel placed between the O3 system of relay lenses and the detector is used to select spectral and polarimetric channels, see Table 2. The filter wheel has six slots (Fig. 11). The main spectral channel is the wideband channel (around 300 Å wide) centered around 5510 Å that is dominated by the emission of the coronal continuum essentially at all temperatures of the emitting plasma[8]. Three slots combine the same wideband channel with polarizers oriented at 0°, 60°, and 120°. Two narrowband channels are also present. One is sensitive to the hot coronal emission formed at temperatures around 2 MK in the Fe XIV line[9] at 5304 Å, see e.g. Del Zanna & DeLuca (2018). The second is sensitive to the emission of prominences in the He I D_3 line at 5877 Å. The He I D_3 line is sensitive to prominence plasma under a range of conditions at temperatures between 8 10^3 K and 10^5 K (Jejčič et al. 2018). The actual spectral profiles are shown in Fig. 14 (see also Table 2).

5.2. Electronics

After the filter wheel, the light comes to the Focal Plane Assembly (FPA), of which the main part is the detector protected by a glass with 50% neutral density filter (to decrease the intensity of optical ghosts). It is an Active Pixel Sensor frontside illuminated detector that has 2048×2048 square pixels, which have 10 μm size and 14 bit output. The same type of detector is mounted on the Metis coronagraph (Antonucci et al. 2020) and on the Polarimetric and Helioseismic Imager (PHI, see Solanki et al. 2020) aboard Solar Orbiter. The detector output is transferred to the Camera Electronic Box (CEB), which controls the detector operations.

The CEB controls the FPA by sending the required control signals, and receiving the analog images taken by the detector and digitizing them. Due to the high dynamic range of the corona and the essentially unvignetted field of view of ASPIICS, the full detector cannot be properly exposed, avoiding both saturation and underexposure. Different exposure times need to be used in different parts of the image. The complete image on the detector is divided into 32×32 tiles, each having 64×64 pixels. Each tile is small enough, so that a single integration time is sufficient to expose it properly. Properly exposed tiles are then selected in the CEB (see Sect. 7). The images are then sent to the Coronagraph Control Box (CCB).

The CCB is the onboard computer that controls all activities of the instrument. It consists of the Power Conditioning Unit

---

[7] Note that the vignetting numbers in Shestov et al. (2021) are slightly different as a different value of the internal occulter radius was assumed in that work.

[8] The wideband channel contains a weak Ar X line at 5533 Å (Del Zanna & DeLuca 2018) that is visible only in the very hot corona (peak formation temperature of 3 MK).

[9] As ASPIICS observes in vacuum, all the wavelengths are listed in vacuum.

Table 2: Spectral passbands of ASPIICS.

Short name	Passband name	Spectral peak	Passband FWHM	Main contributions
WBF	Wideband	5510.6 Å	295.5 Å	continuum
Pol 0	Wideband + polarizer at 0°	5519.3 Å	296.3 Å	polarized continuum
Pol 60	Wideband + polarizer at 60°	5507.3 Å	295.6 Å	polarized continuum
Pol 120	Wideband + polarizer at 120°	5512.9 Å	295.9 Å	polarized continuum
Fe XIV	Narrowband Fe XIV	5303.4 Å	5.4 Å	coronal green line (Fe XIV, 5304 Å) and continuum
He I	Narrowband He I D$_3$	5876.1 Å	21.0 Å	He I D$_3$ line in prominences, continuum
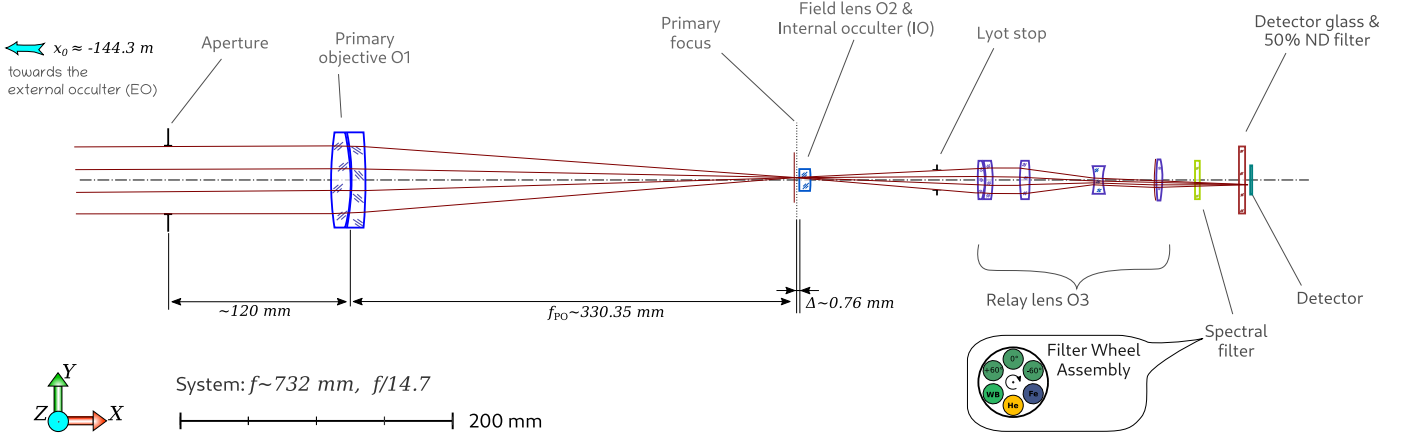
Fig. 11: Optical scheme of the ASPIICS instrument.

(PCU), Ancillary Electronics Unit (AEU), and the Data Processing Unit (DPU). The PCU provides power to all subsystems of the coronagraph. AEU operates the instrument door, the filter wheel, the Shadow Position Sensor (SPS, see Sect. 5.3), and sends the commands to the CEB. The DPU interfaces with the central computer of the CSC, receives the ASPIICS data from the CEB, compresses them using an CCSDS 121.0-B-2 FPGA accelerator (Kranitis et al. 2015), and sends them to the spacecraft mass memory. All three CCB subsystems have two nearly identical units for redundancy.

5.3. Formation flying metrology

In addition to the spacecraft formation flying metrologies described in Sect. 4, ASPIICS makes use of two additional metrologies: the Shadow Position Sensor (SPS) and the Occulter Position Sensor Emitter (OPSE). The SPS is used to determine the precise position of the ASPIICS entrance aperture with respect to the umbra produced by the external occulter. The OPSE is used to determine the position of the external occulter in the coronagraph field of view.

5.3.1. Shadow Position Sensor (SPS)

The Shadow Position Sensor (SPS, see Loreggia et al. 2018; Noce et al. 2021) represents a set of eight photodiodes around the entrance aperture of ASPIICS (Fig. 15). The difference between the readings of different photodiodes is used by an onboard algorithm within the ASPIICS software to estimate the degree of de-centering of the ASPIICS aperture with respect to the umbra produced by the external occulter. This information is used by the spacecraft and the required action is taken: either adjustment of the CSC position, or closing of the ASPIICS door (in case the de-centering is important enough to present a danger of direct sunlight entering the instrument aperture).

The photodiodes are placed in the penumbra of the external occulter, along a circle with the radius of 55 mm centered at the ASPIICS entrance aperture. Eight photodiodes are used, organized in two sets (nominal and redundant) of four photodiodes. The algorithm of the SPS is described by (Casti et al. 2019). The designed accuracy of SPS to determine the lateral displacement of the ASPIICS entrance aperture with respect to its nominal position in the umbra is 50 μm.

5.3.2. Occulter Position Sensor Emitter (OPSE)

The Occulter Position Sensor Emitter (OPSE) is a set of three light emitters mounted on the rear side of the OSC (the side facing the CSC), see Fig. 5. They can be directly imaged by ASPIICS due to a hole in its internal occulter (the hole diameter is 1.085 mm). The purpose of OPSE is thus to determine the position of the external occulter with respect to the coronagraph and to verify the alignment of the two spacecraft. The three emitters are arranged in a pattern of a scalene right triangle (Fig. 5, right panel), so that an image of OPSE gives unambiguous information about the position of the external occulter in the ASPIICS field of view. Information about the inter-satellite distance and the tilt of the external occulter can also be deduced. It has been
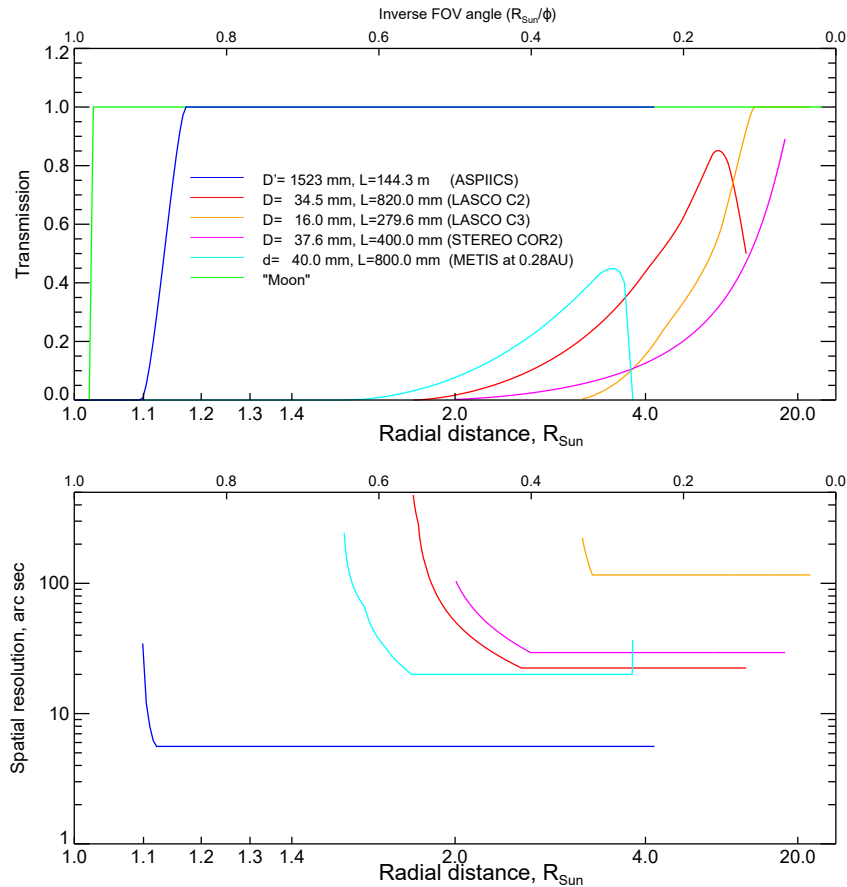
Fig. 12: Top panel: comparison of vignetting functions of modern externally occulted coronagraphs and the Moon. Bottom panel: comparison of spatial resolutions of modern externally occulted coronagraphs. Despite the angular resolution of Metis (20″ in the unvignetted zone) being worse than that of ASPIICS (2.817″ in the unvignetted zone), the linear spatial resolutions of ASPIICS and Metis are very similar (around 4000 km) when Metis observes the Sun from a vantage point near the Solar Orbiter perihelion at 0.28 au.

shown that the straylight produced by the OPSE that reaches the ASPIICS detector through the hole in the internal occulter is negligible (Galy et al. 2019).

The information that can be derived from OPSE is not used onboard for formation flying adjustment, but is used a posteriori on the ground for the analysis of the images.

Each of the three OPSE emitters consists of two diodes (one nominal and one redundant). The designed precision of the determination of the position of the external occulter using OPSE is 0.3 mm.

6. Instrument performance

Assembly and the first part of the on-ground calibration of ASPI-ICS were done at the Centre Spatial de Liège, Belgium, between November 2020 and February 2021 (Galy et al. 2023). The second part of calibration was performed at OPSys facility, Turin, Italy (Capobianco et al. 2019; Fineschi et al. 2025), in September 2021.

During the assembly, the optimal focusing of the telescope was achieved by adjusting the position of the detector along its optical axis. The width of the point spread function (PSF) was measured, and its typical full width at half maximum (FWHM) was around 11.86 μm (the value was slightly different for different angles and different spectral filters), coinciding well with the FWHM of 11.16 μm of a diffraction-limited system (Galy et al.

2023). The pixel plate scale was precisely measured by rotating the telescope at angle ±0.7° and measuring displacement of the collimator cross on the detector. The measured value was 2.817″ per pixel (Galy et al. 2023).

The second part of the calibration was performed at Turin, at the OPSys facility (Capobianco et al. 2019). The following characteristics were measured: detector dark current and bias, radiometric sensitivity, flat field, detector nonlinearity, orientation of polarizers, and level of noise. In general, majority of the measured characteristics and the instrument performance coincided well with the model values (see, for example, Fineschi et al. 2025; Shestov et al. 2021). The radiometric sensitivity was measured by illuminating ASPIICS with a LED-based (light-emitting diode) flat-field panel (FFP), situated few tens of centimeters in front of the entrance aperture. The signal from ASPI-ICS images averaged over the useful field of view was divided by the absolute brightness of the FFP in a corresponding spectral passband. In order to convert the measured values to the mean solar brightness (MSB), the solar spectrum[10] was multiplied with the spectral passbands of ASPIICS (see Fig. 14). Table 3 summarizes the values of the radiometric sensitivity[11].

---

[10] We used the Air Mass Zero (AM0) model, see https://www.nrel.gov/grid/solar-resource/spectra.

[11] In Fineschi et al. (2025) slightly different numbers for the radiometric sensitivity were reported, which differ mainly due to the use of the Planck function to compute the MSB values.
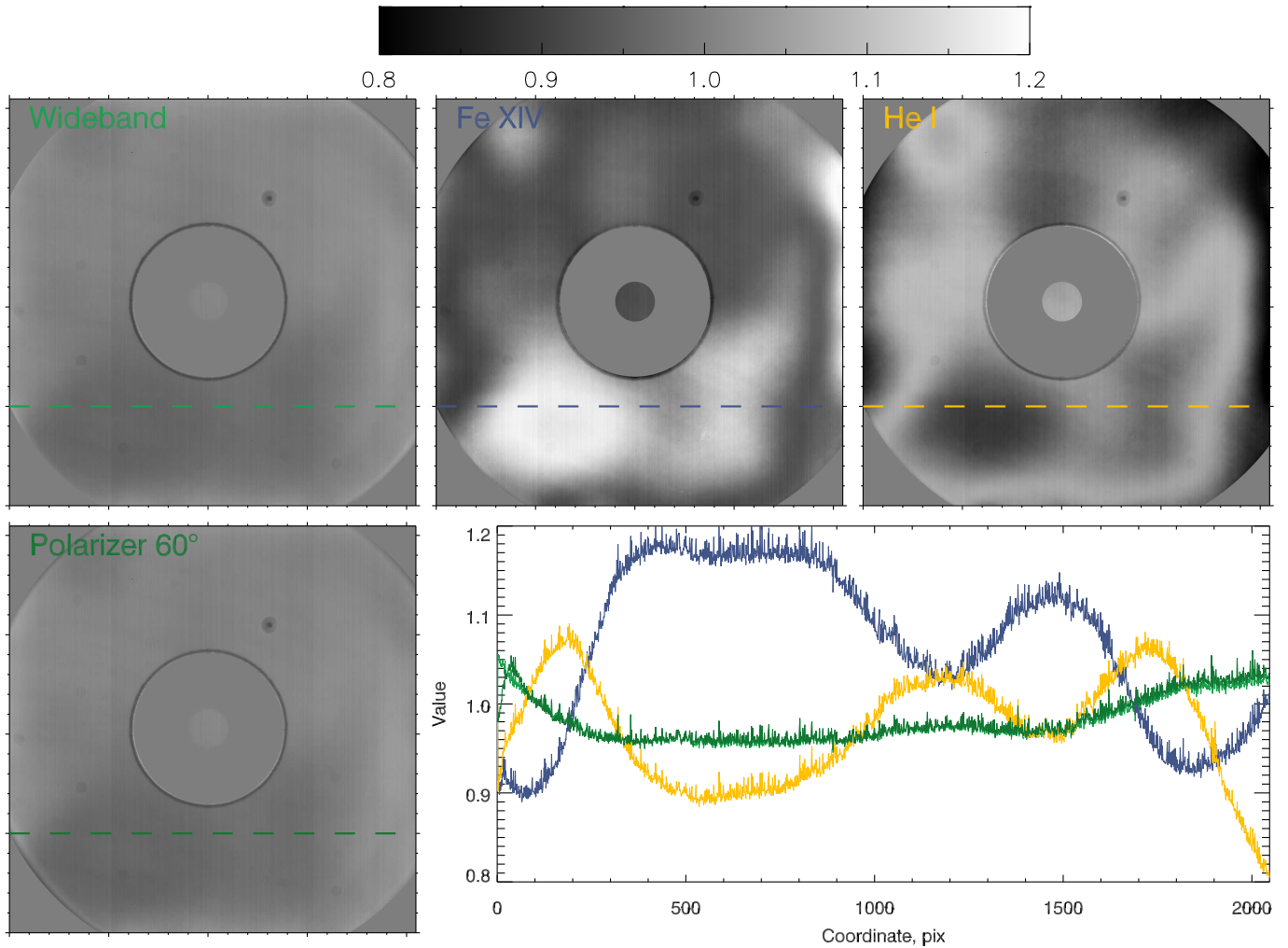
Fig. 13: Flat fields for different spectral channels of ASPIICS measured during the on-ground calibration. The flat fields for the other two polarized channels are very similar to the flat fields of the Wideband and Polarizer 60° channels and are not shown. Note the image of the internal occulter, the hole in the internal occulter, and the vignetted corners of the field of view. The plot in the bottom right panel shows the horizontal profiles along the lines shown in the other panels.

We note that simplification of either of the factors – use of a Plank function instead of AM0, or use of analytical functions (a Gaussian or a box-car) for the spectral passbands of ASPIICS – resulted in a discrepancy of the order of only a few percent as compared to the actually used model.

Variation of the telescope sensitivity across the field of view – the flat field – is shown in Fig. 13 for the wideband, Fe XIV, He I and Polarizer 60° channels. The color scale of the images corresponds to the range 0.8–1.2. The flat fields are normalized in such a way that the average across the useful field of view equals unity; in the region under the IO, and in the vignetting zone it is manually set to unity. The variations of the flat field for the wideband and polarized channels of ASPIICS do not exceed a few percent, and are mainly accounted for by the slight variation of the sensitivity of the detector and the presence of dust particles inside the instrument.

The detector nonlinearity is attributed to the nonlinear conversion of the photo-electrons into the DN (Digital Numbers). The nonlinearity function, defined as the ratio of the measured and the linear response minus one, did not exceed 1% across the most of the dynamic range. The random noise, which is a sum of the detector read-out noise, photon and dark current shot noises (Shestov et al. 2021), ranges from ~ 7 DN for minimal exposure (thus being a read-out noise) to ~ 30 DN for the exposures approaching saturation of the detector.

Measurements of the polarizers orientation were performed with an additional pre-polarizer placed between the FFP and the

Table 3: Radiometric sensitivity of ASPIICS

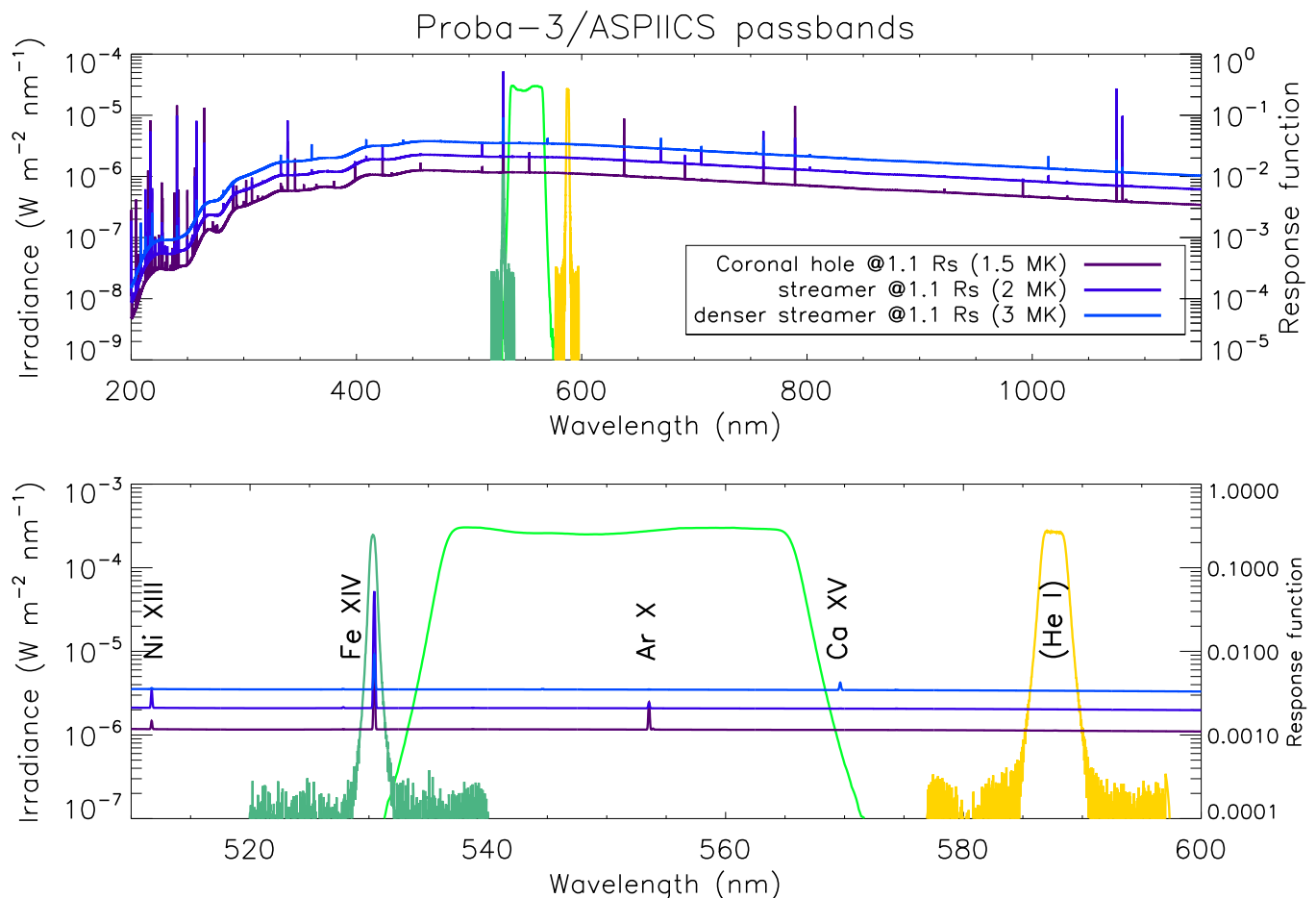| Filter	Absolute radiometric sensitivity, DN cm^2 sr photon^{-1}	MSB value, photon s^{-1} cm^{-2} sr^{-1}	Radiometric sensitivity, DN s^{-1} MSB^{-1}
WBF	1.13×10^{-10}	2.082×10^{20}	2.36×10^{10}
Pol 0	1.01×10^{-10}	2.082×10^{20}	2.11×10^{10}
Pol 60	1.00×10^{-10}	2.082×10^{20}	2.09×10^{10}
Pol 120	9.06×10^{-11}	2.082×10^{20}	1.89×10^{10}
Fe XIV	9.71×10^{-11}	3.742×10^{18}	3.63×10^{8}
He I	1.15×10^{-10}	1.548×10^{19}	1.78×10^{9}

Fig. 14: Top panel: three spectral passbands of ASPIICS (dark green, light green, and yellow curves) plotted on top of the calculated coronal spectrum for three temperatures: 1.5 MK (corresponding to a cooler plasma, e.g. that of a coronal hole), 2 MK (streamer), and 3 MK (hot and dense streamer). Bottom panel shows a narrower spectral range with the main spectral lines marked. The dark green, green, and yellow curves in both panels show the spectral responses of the Fe XIV, WBF, and He I passbands of ASPIICS.

telescope. The pre-polarizer was rotated in small steps, and during subsequent data analysis the parameters of ASPIICS polarizers were calculated on the per-pixel basis. These data were interpreted either as a variation of the polarizer orientation across the FOV (Shestov et al., 2025, in preparation), or as a demodulation tensor for every pixel across the FOV (Casti et al. 2018; Fineschi et al. 2025), with both approaches giving consistent results. The averaged angles of the polarizers amounted to 5.3, 65.6 and 125.4° with a variation up to ±0.5° across the field of view.

Due to the difficulties related to the measurement of the diffracted light in ASPIICS, it was not measured on-ground. Instead, we rely on the theoretical models (Aime 2013; Rougeot et al. 2017; Shestov & Zhukov 2018).

7. Operational concept

7.1. Tile maps

In order to match the very large dynamic range of brightness in the corona, images will be recombined onground from up to 3 consecutive frames taken in the same passband with different exposure times. To avoid downlinking underexposed or overex-

posed tiles in a frame to the ground, two approaches will be combined.

First, predefined tile maps specify which tiles must be kept for a given exposure. These tile maps are compound of 1024 tiles, 64×64 pixels each. The tile maps will define three overlapping nearly circular concentric domains with different distances from the solar centre (Fig. 16). The use of tile maps with a reduced number of tiles accelerates the transfer of the recorded images from the camera to the instrument computer (the transfer speed is constant, amounting to 192 tiles per second). Together with reducing the size of the stored data, it therefore favors the achievement of faster observation cadences.

Second, tiles can be discarded depending on the quality flag. The quality flag is applied to each individual tile that is selected by the tile map in the previous step. It introduces no significant delay in the processing of the data, but does not accelerate this processing either (the transfer speed from the camera to the instrument computer being the limiting factor). The quality flag is defined by a set of 3 parameters: the value in DN in the raw image above which a pixel should be deemed not underexposed (*underexposure threshold*, for example above the level of expected dark current), the value in DN above which the pixel is considered saturated or too close to the saturation level (*over-*
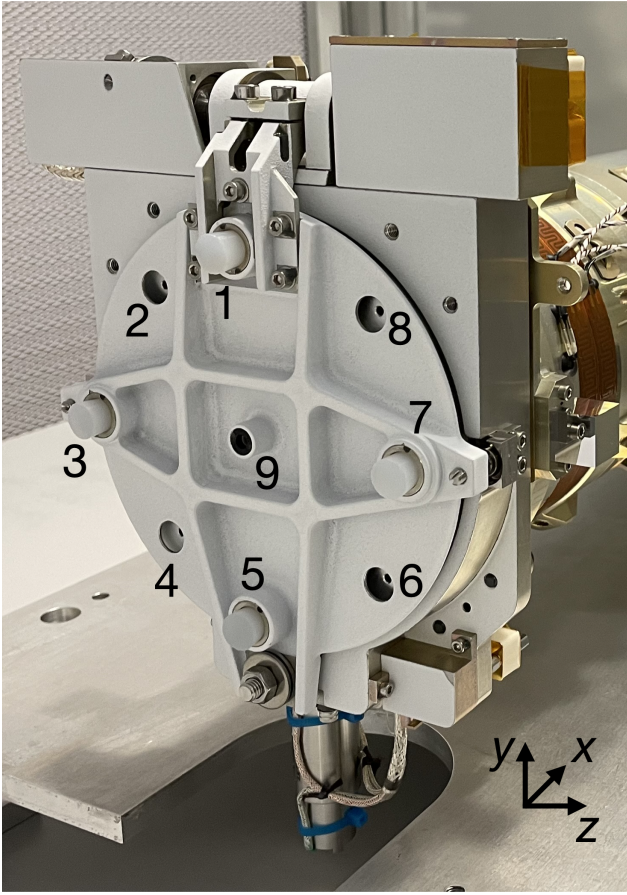
Fig. 15: A photo of the Front Door Assembly (FDA). The annotations highlight the locations of the SPS photo-diodes (nominal set: 1, 3, 5, 7; redundant set: 2, 4, 6, 8) and the high-density diffuser (9). The axes of the coordinate system attached to the instrument are shown, see definition in the caption of Fig. 9.

Table 4: ASPIICS data products.

Data level	Data products	Units[a]
Level-1	Wideband	DN
	Polarizer 0°	DN
	Polarizer 60°	DN
	Polarizer 120°	DN
	Fe XIV passband	DN
	He I D$_3$ passband	DN
Level-2	Wideband	MSB
	Polarizer 0°	MSB
	Polarizer 60°	MSB
	Polarizer 120°	MSB
	Fe XIV passband	MSB
	He I D$_3$ passband	MSB
Level-3	Total brightness	MSB
	Polarized brightness	MSB
	Fe XIV line emissivity	photons s^{-1} cm^{-2} sr^{-1}
	He I D$_3$ line emissivity	photons s^{-1} cm^{-2} sr^{-1}

[a] DN: Data Number; MSB: Mean Solar Brightness.

exposure threshold), and the minimum number of pixels in the tile that should be present between the previous two thresholds (*quality threshold*). If the number of "correctly exposed" pixels is larger than the quality threshold, then the tile is transferred to the instrument computer. Used in combination with "conservative" tile maps (with a lot of overlapping between the tile maps of different exposure times, see Fig. 16), the quality flag automatically adjusts to the generally asymmetric corona and further saves storage space in the onboard mass memory. The extreme case is that of the prominences in He I D$_3$ images, where only a few tiles will contain significant signal with the exposure times that will be typically used, at the location of prominences.

7.2. Observing programs

The camera can take up to 3 successive *exposures* in burst mode, with minimal delay between them (exposure time and detector readout). They are meant to capture the high dynamic range of the corona with, typically, exposure times separated by a factor 10. Together, they form one *acquisition* obtained with the same filter. Each image/exposure can be associated to a different tile map, and each acquisition can be associated with a different set of quality flag parameters. Between each acquisition, the filter wheel can optionally be rotated to change the filter.

Acquisitions can be grouped in a sequence of up to six (corresponding to the 6 different ASPIICS filters), and repeated a

certain number of times (a *cycle*), to build the *observing programs*.

The observing programs are fully flexible, but a minimal set of 4 programs is intended to match the ASPIICS science objectives:

1. The *Full Set* program corresponds to a sequence of 6 acquisitions, one for each filter, with 2 or 3 exposure times for each, to capture the dynamic range of the coronal signal at the best signal-to-noise ratio. It takes a bit less than 4 minutes to complete and is typically intended to observe the quiescent corona (as it includes long exposure times), usually at the beginning and end of each 6-hour coronagraphy interval.

2. The *Synoptic* program consists of a Full Set followed by 54 acquisitions in the wideband filter at a cadence of 60 s (or alternatively, 106 acquisitions at a cadence of 30 s). It lasts 1 hour and can be repeated 6 times to fill in one coronagraphy interval.

3. The *Waves* programs consist of fast cadence observations in one filter (usually wideband), typically at 2 s, 4 s or 15 s cadence, depending on the number of exposures and number of tiles in the tile maps (adapting the field of view accordingly for the desired signal-to-noise ratio).

4. The *CME-Watch* program consists of the wideband and narrowband filters observed every 60 s, replaced by acquisitions in the 3 polarized filters every 5 minutes.

The Waves and CME-Watch programs produce much more data volume in 6 hours than can be downloaded in one day, so that one needs to alternate them with programs producing less data, or use selective downlink.

7.3. Data products

The ASPIICS data products are stored and shared as FITS (Flexible Image Transport System) files in 3 different levels of processing.

Level-1 is the reference dataset that is maximally documented by all available metadata. It keeps the original image
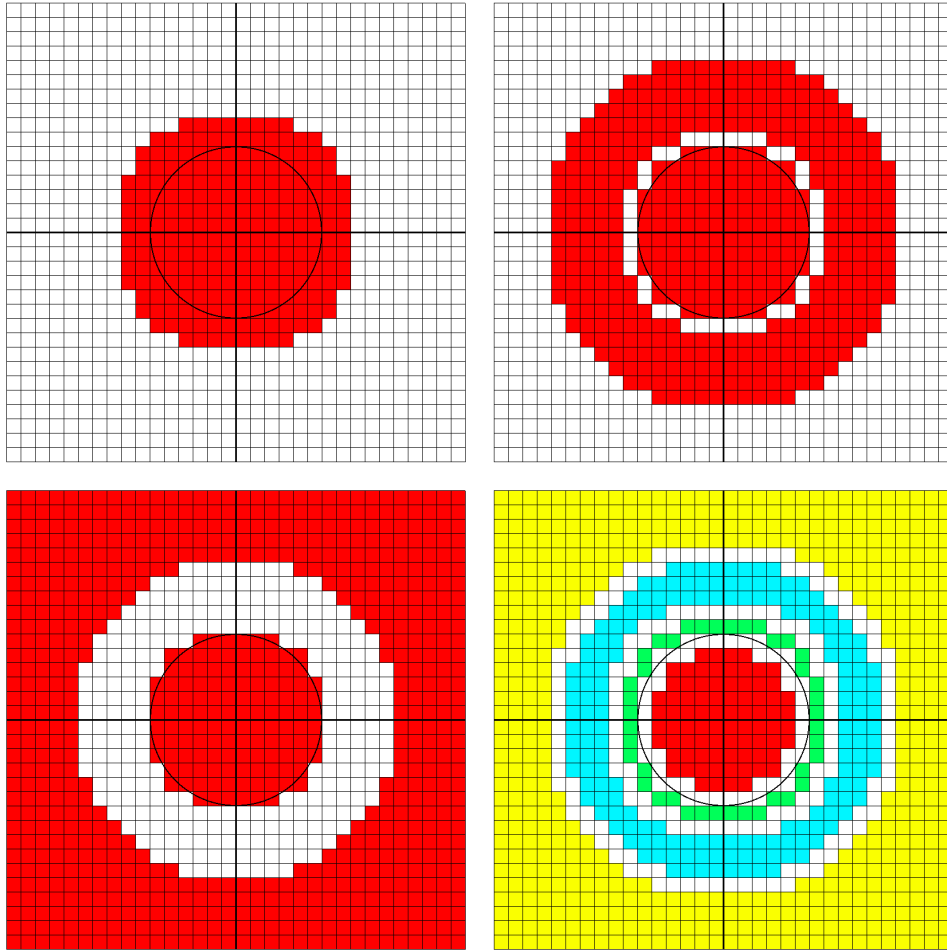
Fig. 16: ASPIICS tile maps. Top left, top right, and bottom left panels show examples of 3 tile maps used to recover the characteristic dynamic range of the coronal brightness in the wideband filter images taken with different exposure times. In these examples, 224, 444, and 756 tiles are retained, shown in red, for Map1, Map2, and Map3, which register the inner, middle and outer parts of the vield of view, respectively. Each tile map is compound of 1024 tiles, 64×64 pixels each. Central tiles are registered in each image to reveal the LEDs of the OPSE. The bottom right panel summarises the tile map regions, with white tiles corresponding to the overlapping tiles which are registered twice in two different exposures to ease their stitching process on the ground.

data untouched and is meant for users with an interest in instrument and calibration issues.

Level-2 is the reference science dataset that is calibrated to the best of the knowledge of the instrument team. It serves most of the needs of the external science community by abstracting as much as possible the instrument peculiarities. At Level-2, each file only contains the data of 1 exposure. Although they contain the full metadata about the position of the Sun in the image and the attitude of the spacecraft, no recentering or rotation is applied to limit interpolation effects.

Level-3 is the dataset that stores derived data products that are optimized for particular scientific purposes. A derived Level-3 image is constructed out of several Level-2 images, at the sacrifice of temporal resolution, and synthetic metadata are added. All exposures of an acquisition are merged to provide the full FOV images with maximal signal-to-noise ratio everywhere. The center of the Sun is set at the center of the image and the image is rotated to have the Solar North up. The continuum component is removed from the narrow passbands, using the information about continuum acquired in the wideband image that is nearest in time.

Table 4 summarizes the ASPIICS data products[12]. The Level-3 data will be also provided as PNG (Portable Network Graphics) images and MPEG (Moving Picture Experts Group) movies. All the ASPIICS data will be freely available in the framework of the open data policy.

8. Summary

Proba-3 is a mission driven by both science and technology. It is first of all a technology demonstration mission: Proba-3 will test precise formation flying techniques and technologies that can be used by future missions. Proba-3 is also a Mission of Opportunity in the ESA Science Programme, as Proba-3/ASPIICS will be a significant advance from previous, current, and planned solar coronagraphs. Due to the unique separation between the telescope and the external occulter (around 144 m), ASPIICS will be able to observe the inner corona as close to the solar centre as 1.099 $R_\odot$ in low straylight conditions. ASPIICS will therefore

---

[12] In addition, there is a Level-0 dataset that contains the science data only with the metadata traveling with the telemetry. It is used as a basis for potential reprocessing and is not publicly available.

fill the gap between the low corona (typically observed by EUV imagers like SDO/AIA) and the high corona (typically observed by externally occulted coronagraphs like SOHO/LASCO C2), where observations are difficult. ASPIICS observations will be crucial for solving several outstanding problems in solar physics, such as structure of the magnetized solar corona, sources of the slow solar wind, onset and early acceleration of coronal mass ejections. ASPIICS heralds the new generation of solar space coronagraphs.

References

Abbo, L., Ofman, L., Antiochos, S. K., et al. 2016, Space Sci. Rev., 201, 55
Aime, C. 2013, A&A, 558, A138
Altrock, R. C. 2004, Sol. Phys., 224, 255
Alzate, N., Di Matteo, S., Morgan, H., Viall, N., & Vourlidas, A. 2024, ApJ, 973, 130
Amari, T., Aly, J. J., Luciani, J. F., Mikic, Z., & Linker, J. 2011, ApJ, 742, L27
Amari, T., Aly, J. J., Mikic, Z., & Linker, J. 2007, ApJ, 671, L189
Antiochos, S. K., DeVore, C. R., & Klimchuk, J. A. 1999, ApJ, 510, 485
Antiochos, S. K., Mikić, Z., Titov, V. S., Lionello, R., & Linker, J. A. 2011, ApJ, 731, 112
Antonucci, E., Romoli, M., Andretta, V., et al. 2020, A&A, 642, A10
Ardaens, J.-S., D'Amico, S., & Cropp, A. 2013, Acta Astronautica, 91, 341
Asensio Ramos, A. 2023, Sol. Phys., 298, 135
Auchère, F., Berghmans, D., Dumesnil, C., et al. 2023a, A&A, 674, A127
Auchère, F., Soubrié, E., Pelouze, G., & Buchlin, É. 2023b, A&A, 670, A66
Bailey, Z., Bandyopadhyay, R., Habbal, S., & Druckmüller, M. 2025, ApJ, 980, L20
Baker, D., Démoulin, P., Yardley, S. L., et al. 2023, ApJ, 950, 65
Banaszkiewicz, M., Axford, W. I., & McKenzie, J. F. 1998, A&A, 337, 940
Banerjee, D., Erdélyi, R., Oliver, R., & O'Shea, E. 2007, Sol. Phys., 246, 3
Bein, B. M., Berkebile-Stoiser, S., Veronig, A. M., et al. 2011, ApJ, 738, 191
Bemporad, A. 2008, ApJ, 689, 572
Bemporad, A. 2023, ApJ, 946, 14
Bemporad, A., Abbo, L., Albert, K., et al. 2025, ApJ, 985, 145
Bemporad, A., Matthaeus, W. H., & Poletto, G. 2008, ApJ, 677, L137
Bemporad, A., Poletto, G., Suess, S. T., et al. 2006, ApJ, 638, 1110
Bemporad, A., Raymond, J., Poletto, G., & Romoli, M. 2007, ApJ, 655, 576
Benavitz, L. F., Boe, B., & Habbal, S. R. 2024, ApJ, 974, 178
Berger, T., Testa, P., Hillier, A., et al. 2011, Nature, 472, 197
Berghmans, D., Auchère, F., Long, D. M., et al. 2021, A&A, 656, L4
Berghmans, D., Hochedez, J. F., Defise, J. M., et al. 2006, Advances in Space Research, 38, 1807
Bąk-Stęślicka, U., Gibson, S. E., Fan, Y., et al. 2013, ApJ, 770, L28
Bothmer, V. & Zhukov, A. 2007, in Space Weather- Physics and Effects, ed. V. Bothmer & I. A. Daglis, 31
Bout, M., Lamy, P., Maucherat, A., Colin, C., & Llebaria, A. 2000, Appl. Opt., 39, 3955
Bradshaw, M. J., Gao, Y., & Homewood, K. 2018, in Society of Photo-Optical Instrumentation Engineers (SPIE) Conference Series, Vol. 10743, Optical Modeling and Performance Predictions X, ed. M. A. Kahan & M. B. Levine-West, 107430H
Brueckner, G. E., Howard, R. A., Koomen, M. J., et al. 1995, Sol. Phys., 162, 357
Bruno, R. & Carbone, V. 2013, Living Reviews in Solar Physics, 10, 2

Canou, A., Amari, T., Bommier, V., et al. 2009, ApJ, 693, L27
Capobianco, G., Fineschi, S., Massone, G., et al. 2019, in Society of Photo-Optical Instrumentation Engineers (SPIE) Conference Series, Vol. 11180, International Conference on Space Optics — ICSO 2018, ed. Z. Sodnik, N. Karafolas, & B. Cugny, 111807M
Carley, E. P., Long, D. M., Byrne, J. P., et al. 2013, Nature Physics, 9, 811
Casti, M., Bemporad, A., Fineschi, S., et al. 2019, in Society of Photo-Optical Instrumentation Engineers (SPIE) Conference Series, Vol. 11180, International Conference on Space Optics — ICSO 2018, ed. Z. Sodnik, N. Karafolas, & B. Cugny, 1118082
Casti, M., Fineschi, S., Capobianco, G., et al. 2018, in Society of Photo-Optical Instrumentation Engineers (SPIE) Conference Series, Vol. 10698, Space Telescopes and Instrumentation 2018: Optical, Infrared, and Millimeter Wave, ed. M. Lystrup, H. A. MacEwen, G. G. Fazio, N. Batalha, N. Siegler, & E. C. Tong, 1069831
Chandran, B. D. G., Quataert, E., Howes, G. G., Xia, Q., & Pongkitiwanichakul, P. 2009, ApJ, 707, 1668
Chen, J., Howard, R. A., Brueckner, G. E., et al. 1997, ApJ, 490, L191
Cheng, X., Zhang, J., Ding, M. D., Liu, Y., & Poomvises, W. 2013, ApJ, 763, 43
Cheng, X., Zhang, J., Kliem, B., et al. 2020, ApJ, 894, 85
Chitta, L. P., Seaton, D. B., Downs, C., DeForest, C. E., & Higginson, A. K. 2023a, Nature Astronomy, 7, 133
Chitta, L. P., Zhukov, A. N., Berghmans, D., et al. 2023b, Science, 381, 867
Ciaravella, A., Raymond, J. C., & Kahler, S. W. 2006, ApJ, 652, 774
Ciaravella, A., Raymond, J. C., Kahler, S. W., Vourlidas, A., & Li, J. 2005, ApJ, 621, 1121
Ciaravella, A., Raymond, J. C., Li, J., et al. 2002, ApJ, 575, 1116
Cirtain, J. W., Golub, L., Lundquist, L., et al. 2007, Science, 318, 1580
Cirtain, J. W., Golub, L., Winebarger, A. R., et al. 2013, Nature, 493, 501
Cliver, E. W., Richardson, I. G., & Martin, S. F. 2025, Geophys. Res. Lett., 52, e2024GL113791
Cliver, E. W., Webb, D. F., & Howard, R. A. 1999, Sol. Phys., 187, 89
Cremades, H. & Bothmer, V. 2004, A&A, 422, 307
Davila, J. M. 1987, ApJ, 317, 514
De Pontieu, B., McIntosh, S. W., Carlsson, M., et al. 2007, Science, 318, 1574
de Wijn, A. G., Burkepile, J. T., Tomczyk, S., et al. 2012, in Society of Photo-Optical Instrumentation Engineers (SPIE) Conference Series, Vol. 8444, Ground-based and Airborne Telescopes IV, ed. L. M. Stepp, R. Gilmozzi, & H. J. Hall, 84443N
Decraemer, B., Zhukov, A. N., & Van Doorsselaere, T. 2019, ApJ, 883, 152
Decraemer, B., Zhukov, A. N., & Van Doorsselaere, T. 2020, ApJ, 893, 78
DeForest, C. E., Erickson, N. F., Beasley, M. N., et al. 2025, ApJ, 982, 58
DeForest, C. E., Howard, R. A., Velli, M., Viall, N., & Vourlidas, A. 2018, ApJ, 862, 18
Del Zanna, G. & DeLuca, E. E. 2018, ApJ, 852, 52
Delannee, C., Koutchmy, S., Veselovsky, I. S., & Zhukov, A. N. 1998, A&A, 329, 1111
Ding, T. & Zhang, J. 2024, ApJ, 974, 104
Domingo, V., Fleck, B., & Poland, A. I. 1995, Sol. Phys., 162, 1
Downs, C., Linker, J. A., Caplan, R. M., et al. 2025, Science, 388, 1306
Druckmüller, M., Habbal, S. R., & Morgan, H. 2014, ApJ, 785, 14
Duan, Y., Shen, Y., Tang, Z., Zhou, C., & Tan, S. 2024, ApJ, 968, 110
Edwards, L., Bunting, K. A., Ramsey, B., et al. 2023, Sol. Phys., 298, 140
Emslie, A. G., Dennis, B. R., Shih, A. Y., et al. 2012, ApJ, 759, 71
Eselevich, M. V. & Eselevich, V. G. 2008, Geophys. Res. Lett., 35, L22105
Fan, Y. & Gibson, S. E. 2003, ApJ, 589, L105
Feldman, U., Widing, K. G., & Warren, H. P. 1999, ApJ, 522, 1133
Feng, L., Inhester, B., & Gan, W. Q. 2013, ApJ, 774, 141
Feng, S. W., Chen, Y., Li, B., et al. 2011, Sol. Phys., 272, 119
Filippov, B. 2024, ApJ, 977, 259
Filippov, B. & Koutchmy, S. 2008, Annales Geophysicae, 26, 3025
Fineschi, S., Zhukov, A., Thizy, C., et al. 2025, in International Conference on Space Optics — ICSO 2024, ed. F. Bernard, N. Karafolas, P. Kubik, & K. Minoglou, Vol. 13699, International Society for Optics and Photonics (SPIE), 136990J
Fisher, R. R., Lee, R. H., MacQueen, R. M., & Poland, A. I. 1981, Appl. Opt., 20, 1094
Forbes, T. G. 2000, J. Geophys. Res., 105, 23153
Fort, B., Morel, C., & Spaak, G. 1978, A&A, 63, 243
Frassati, F., Bemporad, A., Mancuso, S., et al. 2024, ApJ, 964, 15
Fuller, J. & Gibson, S. E. 2009, ApJ, 700, 1205
Galano, D., Bemporad, A., Buckley, S., et al. 2018, in Society of Photo-Optical Instrumentation Engineers (SPIE) Conference Series, Vol. 10698, Space Telescopes and Instrumentation 2018: Optical, Infrared, and Millimeter Wave, ed. M. Lystrup, H. A. MacEwen, G. G. Fazio, N. Batalha, N. Siegler, & E. C. Tong, 106982Y
Galy, C., Fineschi, S., Galano, D., et al. 2015, in Society of Photo-Optical Instrumentation Engineers (SPIE) Conference Series, Vol. 9604, Solar Physics and Space Weather Instrumentation VI, ed. S. Fineschi & J. Fennelly, 96040B

Galy, C., Thizy, C., Stockman, Y., et al. 2019, in Society of Photo-Optical Instrumentation Engineers (SPIE) Conference Series, Vol. 11180, International Conference on Space Optics — ICSO 2018, ed. Z. Sodnik, N. Karafolas, & B. Cugny, 111802H

Galy, C., Thizy, C., Versluys, J., et al. 2023, in Society of Photo-Optical Instrumentation Engineers (SPIE) Conference Series, Vol. 12777, Society of Photo-Optical Instrumentation Engineers (SPIE) Conference Series, ed. K. Minoglou, N. Karafolas, & B. Cugny, 1277767

Gary, D. E. 2023, ARA&A, 61, 427

Gary, G. A. 2001, Sol. Phys., 203, 71

Gibson, S. 2015, in Astrophysics and Space Science Library, Vol. 415, Solar Prominences, ed. J.-C. Vial & O. Engvold, 323

Gibson, S. E. 2018, Living Rev. Sol. Phys., 15, 7

Gibson, S. E., Foster, D., Burkepile, J., de Toma, G., & Stanger, A. 2006, ApJ, 641, 590

Gopalswamy, N., Thompson, W. T., Davila, J. M., et al. 2009, Sol. Phys., 259, 227

Gosling, J. T. 1993, J. Geophys. Res., 98, 18937

Gosling, J. T., Borrini, G., Asbridge, J. R., et al. 1981, J. Geophys. Res., 86, 5438

Harrison, R. A. 1996, Sol. Phys., 166, 441

Heinzel, P., Jejčič, S., Štěpán, J., et al. 2023, ApJ, 957, L10

Heinzel, P., Schmieder, B., Fárník, F., et al. 2008, ApJ, 686, 1383

Higginson, A. K., Antiochos, S. K., DeVore, C. R., Wyper, P. F., & Zurbuchen, T. H. 2017, ApJ, 837, 113

Hoeksema, J. T., Wilcox, J. M., & Scherrer, P. H. 1983, J. Geophys. Res., 88, 9910

Hollweg, J. V. 1971, J. Geophys. Res., 76, 5155

Howard, R. A., Moses, J. D., Vourlidas, A., et al. 2008, Space Sci. Rev., 136, 67

Hundhausen, J. R. & Low, B. C. 1994, ApJ, 429, 876

Illing, R. M. E. & Hundhausen, A. J. 1986, J. Geophys. Res., 91, 10951

Jain Jacob, P. T. & Maurya, R. A. 2025, Journal of Geophysical Research (Space Physics), 130, 2024JA033479

Jarry, M., Rouillard, A. P., Plotnikov, I., Kouloumvakos, A., & Warmuth, A. 2023, A&A, 672, A127

Jejčič, S., Heinzel, P., Labrosse, N., et al. 2018, Sol. Phys., 293, 33

Jess, D. B., Mathioudakis, M., Erdélyi, R., et al. 2009, Science, 323, 1582

Jiang, C., Feng, X., Liu, R., et al. 2021, Nature Astronomy, 5, 1126

Jones, S. I. & Davila, J. M. 2009, ApJ, 701, 1906

Jones, S. I., Davila, J. M., & Uritsky, V. 2016, ApJ, 820, 113

Kaiser, M. L., Kucera, T. A., Davila, J. M., et al. 2008, Space Sci. Rev., 136, 5

Karpen, J. T., Antiochos, S. K., & DeVore, C. R. 2012, ApJ, 760, 81

Kerdraon, A. & Delouis, J.-M. 1997, in Coronal Physics from Radio and Space Observations, ed. G. Trottet, Vol. 483, 192

Kim, I. S. 1997, in NATO Advanced Study Institute (ASI) Series C, Vol. 494, Theoretical and Observational Problems Related to Solar Eclipses, ed. Z. Mouradian & M. Stavinschi, 159–163

Kliem, B., Lin, J., Forbes, T. G., Priest, E. R., & Török, T. 2014, ApJ, 789, 46

Kliem, B. & Török, T. 2006, Phys. Rev. Lett., 96, 255002

Klimchuk, J. A. 2006, Sol. Phys., 234, 41

Ko, Y.-K., Raymond, J. C., Lin, J., et al. 2003, ApJ, 594, 1068

Koutchmy, S. 1971, A&A, 13, 79

Koutchmy, S. 1988, Space Sci. Rev., 47, 95

Koutchmy, S., Belmahdi, M., Coulter, R. L., et al. 1994, A&A, 281, 249

Koutchmy, S. & Fagot, J. 1973, Nature, 246, 414

Koutchmy, S., Picat, J. P., & Dantel, M. 1977, A&A, 59, 349

Koutchmy, S., Slemzin, V., Filippov, B., et al. 2008, A&A, 483, 599

Kranitis, N., Sideris, I., Tsigkanos, A., et al. 2015, Journal of Applied Remote Sensing, 9, 097499

Lamy, P., Damé, L., Vivès, S., & Zhukov, A. 2010, in Society of Photo-Optical Instrumentation Engineers (SPIE) Conference Series, Vol. 7731, Space Telescopes and Instrumentation 2010: Optical, Infrared, and Millimeter Wave, ed. J. M. Oschmann, Jr., M. C. Clampin, & H. A. MacEwen, 773118

Lamy, P., Llebaria, A., Boclet, B., et al. 2020, Sol. Phys., 295, 89

Lamy, P., Vivès, S., Koutchmy, S., & Arnaud, J. 2007, in Astronomical Society of the Pacific Conference Series, Vol. 368, The Physics of Chromospheric Plasmas, ed. P. Heinzel, I. Dorotovič, & R. J. Rutten, 639

Landi Degl'Innocenti, E. & Landolfi, M. 2004, Polarization in Spectral Lines, Vol. 307

Landini, F., Vives, S., Venet, M., et al. 2011, Appl. Opt., 50, 6632

Lemaire, J. 2010, in American Institute of Physics Conference Series, Vol. 1216, Twelfth International Solar Wind Conference, ed. M. Maksimovic, K. Issautier, N. Meyer-Vernet, M. Moncuquet, & F. Pantellini, 8–13

Lemen, J. R., Title, A. M., Akin, D. J., et al. 2012, Sol. Phys., 275, 17

Lenskii, A. V. 1981, Soviet Ast., 25, 366

Lin, J. & Forbes, T. G. 2000, J. Geophys. Res., 105, 2375

Lin, J., Li, J., Forbes, T. G., et al. 2007, ApJ, 658, L123

Linker, J. A., Mikić, Z., Biesecker, D. A., et al. 1999, J. Geophys. Res., 104, 9809

Lionello, R., Linker, J. A., & Mikić, Z. 2009, ApJ, 690, 902

Liu, W. & Ofman, L. 2014, Sol. Phys., 289, 3233

Liu, W., Title, A. M., Zhao, J., et al. 2011, ApJ, 736, L13

Llorente, J. S., Agenjo, A., Carrascosa, C., et al. 2013, Acta Astronautica, 82, 38

Loreggia, D., Fineschi, S., Bemporad, A., et al. 2018, in Society of Photo-Optical Instrumentation Engineers (SPIE) Conference Series, Vol. 10695, Optical Instrument Science, Technology, and Applications, ed. N. Haverkamp & R. N. Youngworth, 1069503

Loucif, M. L. & Koutchmy, S. 1989, A&AS, 77, 45

Low, B. C. 1996, Sol. Phys., 167, 217

Low, B. C. & Hundhausen, J. R. 1995, ApJ, 443, 818

Lu, L., Inhester, B., Feng, L., Liu, S., & Zhao, X. 2017, ApJ, 835, 188

Lynch, B. J. 2020, ApJ, 905, 139

Lynch, B. J., Antiochos, S. K., DeVore, C. R., Luhmann, J. G., & Zurbuchen, T. H. 2008, ApJ, 683, 1192

Lynch, B. J., Wyper, P. F., Palmerio, E., et al. 2025, ApJS, 277, 40

Lyu, S., Wang, Y., Li, X., Zhang, Q., & Liu, J. 2024, ApJ, 962, 170

MacQueen, R. M. & Fisher, R. R. 1983, Sol. Phys., 89, 89

Magdalenić, J., Marqué, C., Zhukov, A. N., Vršnak, B., & Veronig, A. 2012, ApJ, 746, 152

Magdalenić, J., Marqué, C., Zhukov, A. N., Vršnak, B., & Žic, T. 2010, ApJ, 718, 266

Maia, D., Vourlidas, A., Pick, M., et al. 1999, J. Geophys. Res., 104, 12507

Majumdar, S., D'Huys, E., Mierla, M., et al. 2024, ApJ, 970, L17

Maričić, D., Vršnak, B., Stanger, A. L., et al. 2007, Sol. Phys., 241, 99

Marqué, C. 2004, ApJ, 602, 1037

McComas, D. J., Elliott, H. A., Schwadron, N. A., et al. 2003, Geophys. Res. Lett., 30, 1517

McIntosh, S. W., de Pontieu, B., Carlsson, M., et al. 2011, Nature, 475, 477

Mierla, M., Schwenn, R., Teriaca, L., Stenborg, G., & Podlipnik, B. 2008, A&A, 480, 509

Mierla, M., Zhukov, A. N., Berghmans, D., et al. 2022, A&A, 662, L5

Mikić, Z., Downs, C., Linker, J. A., et al. 2018, Nature Astronomy, 2, 913

Moore, R. L., Sterling, A. C., Hudson, H. S., & Lemen, J. R. 2001, ApJ, 552, 833

Morgan, H., Habbal, S. R., & Woo, R. 2006, Sol. Phys., 236, 263

Morton, R. J., Molnar, M., Cranmer, S. R., & Schad, T. A. 2025, ApJ, 982, 104

Nakariakov, V. M. & Verwichte, E. 2005, Living Reviews in Solar Physics, 2, 3

Ngampoopun, N., Susino, R., Brooks, D. H., et al. 2025, Sol. Phys., 300, 45

Nikolskiy, G. M., Simonov, A. I., Kim, I. S., et al. 1977, in Apollo-Soyuz Test Project Summary Science Report, NASA SP-412, Vol. 1, 85–99

Noce, V., Loreggia, D., Capobianco, G., et al. 2021, Advances in Space Research, 67, 3807

Noci, G., Kohl, J. L., Antonucci, E., et al. 1997, in ESA Special Publication, Vol. 404, Fifth SOHO Workshop: The Corona and Solar Wind Near Minimum Activity, ed. A. Wilson, 75

November, L. J. & Koutchmy, S. 1996, ApJ, 466, 512

Okamoto, T. J., Tsuneta, S., Berger, T. E., et al. 2007, Science, 318, 1577

Olmedo, O. & Zhang, J. 2010, ApJ, 718, 433

Ontiveros, V. & Vourlidas, A. 2009, ApJ, 693, 267

Paouris, E., Stenborg, G., Linton, M. G., et al. 2024, ApJ, 964, 139

Parenti, S., Schmieder, B., Heinzel, P., & Golub, L. 2012, ApJ, 754, 66

Pariat, E., Antiochos, S. K., & DeVore, C. R. 2009, ApJ, 691, 61

Parker, E. N. 1988, ApJ, 330, 474

Parker, E. N. 2010, in American Institute of Physics Conference Series, Vol. 1216, Twelfth International Solar Wind Conference, ed. M. Maksimovic, K. Issautier, N. Meyer-Vernet, M. Moncuquet, & F. Pantellini, 3–7

Patel, R., Pant, V., Chandrashekhar, K., & Banerjee, D. 2020, A&A, 644, A158

Pellegrin-Frachon, T., Masson, S., Pariat, É., Wyper, P. F., & DeVore, C. R. 2023, A&A, 675, A55

Pesnell, W. D., Thompson, B. J., & Chamberlin, P. C. 2012, Sol. Phys., 275, 3

Peters, T. V., Branco, J., Escorial, D., Castellani, L. T., & Cropp, A. 2014, Acta Astronautica, 102, 296

Plunkett, S. P., Vourlidas, A., Šimberová, S., et al. 2000, Sol. Phys., 194, 371

Pneuman, G. W. & Kopp, R. A. 1971, Sol. Phys., 18, 258

Priest, E. R. 1988, ApJ, 328, 848

Rachmeler, L. A., Gibson, S. E., Dove, J. B., DeVore, C. R., & Fan, Y. 2013, Sol. Phys., 288, 617

Rachmeler, L. A., Platten, S. J., Bethge, C., Seaton, D. B., & Yeates, A. R. 2014, ApJ, 787, L3

Ramesh, R., Muthu Priyal, V., Singh, J., et al. 2024, ApJ, 976, L6

Raymond, J. C., Ciaravella, A., Dobrzycka, D., et al. 2003, ApJ, 597, 1106

Renotte, E., Baston, E. C., Bemporad, A., et al. 2014, in Society of Photo-Optical Instrumentation Engineers (SPIE) Conference Series, Vol. 9143, Space Telescopes and Instrumentation 2014: Optical, Infrared, and Millimeter Wave, ed. J. M. Oschmann, Jr., M. Clampin, G. G. Fazio, & H. A. MacEwen, 91432M

Rochus, P., Auchère, F., Berghmans, D., et al. 2020, A&A, 642, A8

Rodríguez-Gómez, J. M., Kuckein, C., González Manrique, S. J., et al. 2024, ApJ, 964, 27

Romano, P., Wyper, P., Andretta, V., et al. 2025, ApJ, 982, 142

Rougeot, R., Aime, C., Baccani, C., et al. 2018, in Society of Photo-Optical Instrumentation Engineers (SPIE) Conference Series, Vol. 10698, Space Telescopes and Instrumentation 2018: Optical, Infrared, and Millimeter Wave, ed. M. Lystrup, H. A. MacEwen, G. G. Fazio, N. Batalha, N. Siegler, & E. C. Tong, 106982T

Rougeot, R., Flamary, R., Galano, D., & Aime, C. 2017, A&A, 599, A2

Roussev, I. I., Lugaz, N., & Sokolov, I. V. 2007, ApJ, 668, L87

Rust, D. M. & Hildner, E. 1976, Sol. Phys., 48, 381

Saez, F., Zhukov, A. N., Lamy, P., & Llebaria, A. 2005, A&A, 442, 351

Saint-Hilaire, P., Krucker, S., & Lin, R. P. 2009, ApJ, 699, 245

Saito, K. & Hyder, C. L. 1968, Sol. Phys., 5, 61

Saito, K. & Tandberg-Hanssen, E. 1973, Sol. Phys., 31, 105

Sakao, T., Kano, R., Narukage, N., et al. 2007, Science, 318, 1585

Schatten, K. H., Wilcox, J. M., & Ness, N. F. 1969, Sol. Phys., 6, 442

Schwenn, R. 2006, Living Reviews in Solar Physics, 3, 2

Schwenn, R., Inhester, B., Plunkett, S. P., et al. 1997, Sol. Phys., 175, 667

Seaton, D. B., Berghmans, D., Nicula, B., et al. 2013, Sol. Phys., 286, 43

Seaton, D. B., Hughes, J. M., Tadikonda, S. K., et al. 2021, Nature Astronomy, 5, 1029

Seaton, D. B., Mierla, M., Berghmans, D., Zhukov, A. N., & Dolla, L. 2011, ApJ, 727, L10

Shaik, S. B., Linton, M. G., Gibson, S. E., et al. 2024, ApJ, 976, 179

Sheeley, N. R., Hakala, W. N., & Wang, Y. M. 2000, J. Geophys. Res., 105, 5081

Sheeley, N. R., Wang, Y. M., Hawley, S. H., et al. 1997, ApJ, 484, 472

Sheeley, Jr., N. R. & Wang, Y. M. 2007, ApJ, 655, 1142

Shestov, S. V. & Zhukov, A. N. 2018, A&A, 612, A82

Shestov, S. V., Zhukov, A. N., Inhester, B., Dolla, L., & Mierla, M. 2021, A&A, 652, A4

Shestov, S. V., Zhukov, A. N., & Seaton, D. B. 2019, A&A, 622, A101

Shi, G., Feng, L., Ying, B., Li, S., & Gan, W. 2024, ApJ, 970, 131

Shibata, K., Ishido, Y., Acton, L. W., et al. 1992, PASJ, 44, L173

Sime, D. G. 1986, in The Sun and the Heliosphere in Three Dimensions, ed. R. G. Marsden & L. A. Fisk, Vol. 123, 45

Sime, D. G. & Hundhausen, A. J. 1987, J. Geophys. Res., 92, 1049

Slemzin, V., Bougaenko, O., Ignatiev, A., et al. 2008, Annales Geophysicae, 26, 3007

Slemzin, V., Harra, L., Urnov, A., et al. 2013, Sol. Phys., 286, 157

Solanki, S. K., del Toro Iniesta, J. C., Woch, J., et al. 2020, A&A, 642, A11

Song, H., Li, L., Wang, B., Xia, L., & Chen, Y. 2025, ApJ, 978, 40

Song, H., Li, L., Zhou, Z., et al. 2023, ApJ, 952, L22

Sorokina, D., Van Doorsselaere, T., Talpeanu, D. C., & Poedts, S. 2024, A&A, 682, A168

St. Cyr, O. C., Burkepile, J. T., Hundhausen, A. J., & Lecinski, A. R. 1999, J. Geophys. Res., 104, 12493

St. Cyr, O. C., Flint, Q. A., Xie, H., et al. 2015, Sol. Phys., 290, 2951

Stenborg, G. & Cobelli, P. J. 2003, A&A, 398, 1185

Sterling, A. C. & Hudson, H. S. 1997, ApJ, 491, L55

Su, Y., Veronig, A. M., Holman, G. D., et al. 2013, Nature Physics, 9, 489

Susino, R., Bemporad, A., & Krucker, S. 2013, ApJ, 777, 93

Tadikonda, S. K., Freesland, D. C., Minor, R. R., et al. 2019, Sol. Phys., 294, 28

Telloni, D., Antonucci, E., Bruno, R., & D'Amicis, R. 2009, ApJ, 693, 1022

Telloni, D., Sorriso-Valvo, L., Zank, G. P., et al. 2024, ApJ, 973, L48

Temmer, M. 2021, Living Reviews in Solar Physics, 18, 4

Temmer, M., Veronig, A. M., Kontar, E. P., Krucker, S., & Vršnak, B. 2010, ApJ, 712, 1410

Thernisien, A., Vourlidas, A., & Howard, R. A. 2009, Sol. Phys., 256, 111

Theys, C., Aime, C., Rougeot, R., & Lantéri, H. 2022, A&A, 665, A109

Thompson, B. J., Plunkett, S. P., Gurman, J. B., et al. 1998, Geophys. Res. Lett., 25, 2465

Titov, V. S. & Démoulin, P. 1999, A&A, 351, 707

Titov, V. S., Mikic, Z., Linker, J. A., & Lionello, R. 2008, ApJ, 675, 1614

Tomczyk, S., Card, G. L., Darnell, T., et al. 2008, Sol. Phys., 247, 411

Tomczyk, S. & McIntosh, S. W. 2009, ApJ, 697, 1384

Tomczyk, S., McIntosh, S. W., Keil, S. L., et al. 2007, Science, 317, 1192

Török, T. & Kliem, B. 2005, ApJ, 630, L97

Török, T., Panasenco, O., Titov, V. S., et al. 2011, ApJ, 739, L63

Trujillo Bueno, J. 2010, in Astrophysics and Space Science Proceedings, Vol. 19, Magnetic Coupling between the Interior and Atmosphere of the Sun, ed. S. S. Hasan & R. J. Rutten, 118

Tu, C.-Y., Zhou, C., Marsch, E., et al. 2005, Science, 308, 519

Uchida, Y., McAllister, A., Strong, K. T., et al. 1992, PASJ, 44, L155

van Ballegooijen, A. A. & Cranmer, S. R. 2008, ApJ, 682, 644

Van Doorsselaere, T., Andries, J., & Poedts, S. 2007, A&A, 471, 311

Vásquez, A. M., Nuevo, F. A., Romoli, M., et al. 2024, Sol. Phys., 299, 165

Veronig, A. M., Dissauer, K., Kliem, B., et al. 2025, arXiv e-prints, arXiv:2505.19228

Veronig, A. M., Podladchikova, T., Dissauer, K., et al. 2018, ApJ, 868, 107

Viall, N. M. & Vourlidas, A. 2015, ApJ, 807, 176

Vives, S., Damé, L., Lamy, P., et al. 2010, in Society of Photo-Optical Instrumentation Engineers (SPIE) Conference Series, Vol. 7731, Space Telescopes and Instrumentation 2010: Optical, Infrared, and Millimeter Wave, ed. J. M. Oschmann, Jr., M. C. Clampin, & H. A. MacEwen, 773147

Vourlidas, A., Lynch, B. J., Howard, R. A., & Li, Y. 2013, Sol. Phys., 284, 179

Vourlidas, A., Wu, S. T., Wang, A. H., Subramanian, P., & Howard, R. A. 2003, ApJ, 598, 1392

Vršnak, B. 2001, J. Geophys. Res., 106, 25249

Vršnak, B. & Cliver, E. W. 2008, Sol. Phys., 253, 215

Vršnak, B., Magdalenić, J., Temmer, M., et al. 2005, ApJ, 625, L67

Wagner, W. J. & MacQueen, R. M. 1983, A&A, 120, 136

Wang, T., Arge, C. N., & Jones, S. I. 2025, Sol. Phys., 300, 46

Wang, Y.-M., Hawley, S. H., & Sheeley, Jr., N. R. 1996, Science, 271, 464

Wang, Y. M. & Hess, P. 2018, ApJ, 859, 135

Wang, Y. M. & Hess, P. 2023, ApJ, 952, 85

Wang, Y. M., Ko, Y. K., & Grappin, R. 2009, ApJ, 691, 760

Wang, Y. M., Sheeley, N. R., & Andrews, M. D. 2002, Journal of Geophysical Research (Space Physics), 107, 1465

Wang, Y. M., Sheeley, N. R., Socker, D. G., Howard, R. A., & Rich, N. B. 2000a, J. Geophys. Res., 105, 25133

Wang, Y. M. & Sheeley, Jr., N. R. 2002, ApJ, 567, 1211

Wang, Y. M., Sheeley, Jr., N. R., & Rich, N. B. 2000b, Geophys. Res. Lett., 27, 149

Wang, Y. M., Sheeley, Jr., N. R., & Rich, N. B. 2007, ApJ, 658, 1340

Wang, Y. M., Sheeley, Jr., N. R., Walters, J. H., et al. 1998, ApJ, 498, L165

Webb, D. F., Burkepile, J., Forbes, T. G., & Riley, P. 2003, Journal of Geophysical Research (Space Physics), 108, 1440

West, M. J., Seaton, D. B., Wexler, D. B., et al. 2023, Sol. Phys., 298, 78

West, M. J., Zhukov, A. N., Dolla, L., & Rodriguez, L. 2011, ApJ, 730, 122

Wiegelmann, T., Petrie, G. J. D., & Riley, P. 2017, Space Sci. Rev., 210, 249

Wiegelmann, T., Schindler, K., & Neukirch, T. 2000, Sol. Phys., 191, 391

Wilkins, C. P., Pontin, D. I., Yeates, A. R., et al. 2025, ApJ, 985, 190

Wolfson, R. & Saran, S. 1998, ApJ, 499, 496

Wu, S. T., Zhang, T. X., Dryer, M., Feng, X. S., & Tan, A. 2005, Space Sci. Rev., 121, 33

Wyper, P. F., Lynch, B. J., DeVore, C. R., et al. 2024, ApJ, 975, 168

Xing, C., Aulanier, G., Cheng, X., Xia, C., & Ding, M. 2024, ApJ, 966, 70

Yeates, A. R., Mackay, D. H., & van Ballegooijen, A. A. 2008, Sol. Phys., 247, 103

Yeates, A. R., Mackay, D. H., van Ballegooijen, A. A., & Constable, J. A. 2010, Journal of Geophysical Research (Space Physics), 115, A09112

Zhang, J. & Dere, K. P. 2006, ApJ, 649, 1100

Zhang, J., Dere, K. P., Howard, R. A., Kundu, M. R., & White, S. M. 2001, ApJ, 559, 452

Zhong, Z., Guo, Y., Wiegelmann, T., Ding, M. D., & Chen, Y. 2023, ApJ, 947, L2

Zhukov, A. N. 2011, Journal of Atmospheric and Solar-Terrestrial Physics, 73, 1096

Zhukov, A. N. & Auchère, F. 2004, A&A, 427, 705

Zhukov, A. N., Saez, F., Lamy, P., Llebaria, A., & Stenborg, G. 2008, ApJ, 680, 1532

Zhukov, A. N. & Veselovsky, I. S. 2007, ApJ, 664, L131

Zhukov, A. N., Veselovsky, I. S., Koutchmy, S., & Delannée, C. 2000, A&A, 353, 786